FINAL REPORT FOR: AFOSR GRANT FA9550-05-1-0183

TRANSONIC CASCADE MEASUREMENTS TO SUPPORT ANALYTICAL MODELING

John K. Eaton
Department of Mechanical Engineering
Stanford University

Paul A. Durbin
Department of Aerospace Engineering
Iowa State University

submitted to:

Attn: Dr. John Schmisseur
Air Force Office of Scientific Research
875 N. Randolph Street
Suite 325, Room 3112
Arlington, VA 22203

Grant start date: 10/1/2004
Grant end date: 9/30/2007
Date of submission: 7/20/2008

REPORT DOCUMENTATION PAGE

Form Approved
OMB No. 0704-0188

1. REPORT DATE *(DD-MM-YYYY)* 20-07-2008	2. REPORT TYPE Final	3. DATES COVERED *(From - To)* 1/10/2004-30/9/2007

4. TITLE AND SUBTITLE
TRANSONIC CASCADE MEASUREMENTS TO SUPPORT ANALYTICAL MODELING

5a. CONTRACT NUMBER

5b. GRANT NUMBER
FA9550-05-1-0183

5c. PROGRAM ELEMENT NUMBER

6. AUTHOR(S)
John K Eaton, Paul A. Durbin

5d. PROJECT NUMBER

5e. TASK NUMBER

5f. WORK UNIT NUMBER

7. PERFORMING ORGANIZATION NAME(S) AND ADDRESS(ES)
Stanford University
128 Encina Commons
Stanford, CA 94305-6032

8. PERFORMING ORGANIZATION REPORT NUMBER

9. SPONSORING / MONITORING AGENCY NAME(S) AND ADDRESS(ES)
USAF/AFRL
AFOSR
875 N Randolph St Suite 3112
Arlington VA 22203

10. SPONSOR/MONITOR'S ACRONYM(S)

11. SPONSOR/MONITOR'S REPORT NUMBER(S) AFRL-SR-AR-TR-08-0495

12. DISTRIBUTION / AVAILABILITY STATEMENT
Distribution A; distribution is unlimited.

13. SUPPLEMENTARY NOTES

14. ABSTRACT

We have developed a set of benchmark experiments and advanced simulation capabilities for the critical problem of turbine blade trailing-edge film cooling. Modern designs produce low cooling flow effectiveness, and improved designs can't be developed because standard turbulence models grossly overpredict the effectiveness. Two experiments were developed to provide detailed mean velocity and turbulence data around a blade trailing edge in low speed flow and high speed flow with full scale Mach and Reynolds numbers. A new implementation of detached eddy simulation has been developed and applied to a trailing edge film cooling geometry. This has shown favorable agreement with the first set of measurements. This report includes the complete results for the low-speed experiment and detached eddy simulation, as well as the results from the transonic experiment which have been obtained to date. The results show the physical reasons behind the low film-cooling effectiveness of practical trailing edge breakouts. They also show that detached eddy simulation can accurately capture these physical effects with careful attention to the implementation of inlet boundary conditions.

15. SUBJECT TERMS

16. SECURITY CLASSIFICATION OF:			17. LIMITATION OF ABSTRACT	18. NUMBER OF PAGES	19a. NAME OF RESPONSIBLE PERSON
a. REPORT	**b. ABSTRACT**	**c. THIS PAGE**			**19b. TELEPHONE NUMBER** *(include area code)*

Standard Form 298 (Rev. 8-98)
Prescribed by ANSI Std. Z39.18

Abstract

We have developed a set of benchmark experiments and advanced simulation capabilities for the critical problem of turbine blade trailing-edge film cooling. Modern designs produce low cooling flow effectiveness, and improved designs can't be developed because standard turbulence models grossly overpredict the effectiveness. Two experiments were developed to provide detailed mean velocity and turbulence data around a blade trailing edge in low speed flow and high speed flow with full scale Mach and Reynolds numbers. A new implementation of detached eddy simulation has been developed and applied to a trailing edge film cooling geometry. This has shown favorable agreement with the first set of measurements. This report includes the complete results for the low-speed experiment and detached eddy simulation, as well as the results from the transonic experiment which have been obtained to date. The results show the physical reasons behind the low film-cooling effectiveness of practical trailing edge breakouts. They also show that detached eddy simulation can accurately capture these physical effects with careful attention to the implementation of inlet boundary conditions.

1 Introduction

Overheating of the trailing edge is a life-limiting factor for modern high-pressure turbine blades, due to the thin geometry and the complex three-dimensional mixing that occurs in that region. In the standard cooling strategy, cooling air from internal passages is blown from breakouts on the pressure side of the blade to protect the trailing edge from hot ambient gasses. However, field testing and lab experiments show that the efficiency of film cooling at the trailing edge is very low, indicating significant mixing of the coolant air with the mainstream flow over the breakout slots. RANS calculations show low mixing and incorrectly high values for the film cooling effectiveness, and it is not possible to improve the designs when the source of the mixing of the trailing edge coolant flow is not well understood. Understanding this mixing is the motive for the present work.

The terminology used herein is as follows. Figure 1 shows the trailing edge breakout geometry used for the experiments and calculations. The opening is referred to as a *break out* and the flow from the opening is called *pressure side bleed*. Cooling air exits from a rectangular *nozzle* in the break out and is expected to form a cooling shield over the surface. The exposed portion of the wall jet is bounded by raised portions of the blade called *lands*. The upper edge of the nozzle is called the *nozzle lip*. It turns out to be important that the thickness of the nozzle lip is comparable to the nozzle opening below it.
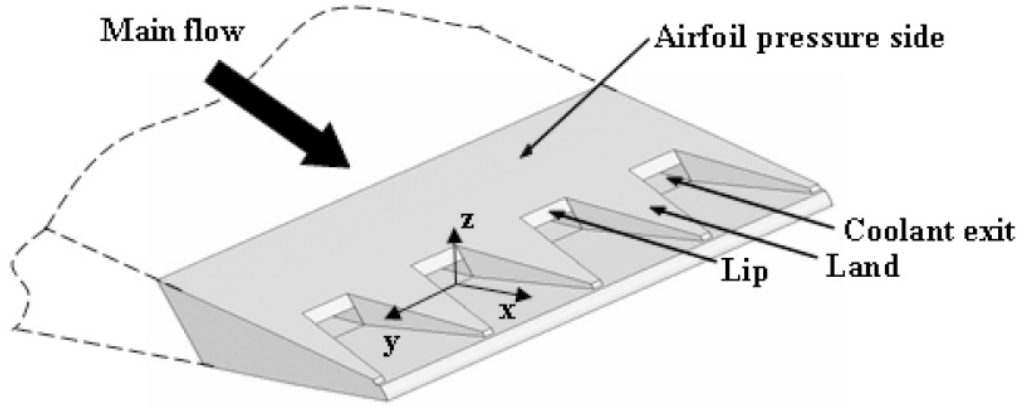
Figure 1: Trailing edge cooling slots at pressure side breakout.

The *adiabatic cooling effectiveness* is the ratio of hot gas temperature minus surface temperature to hot gas minus coolant temperature:

$$\eta = \frac{T_\infty - T_{aw}}{T_\infty - T_c},$$

(1)

If the surface is maintained at the coolant temperature this is unity; as the surface heats up, it decreases. The aim of film cooling is to keep η near unity, and it seems intuitive that such high values would be expected in the space between the lands. Unfortunately, laboratory tests show that the film cooling effectiveness decreases significantly from the coolant exit to the tip of the trailing edge. Holloway et al. [1,2] presented film-cooling effectiveness measurements for a breakout geometry similar to Figure 1. They found that η was considerably below 1.0, with the lowest measured value being around 0.4. They compared their results to computations using both steady and unsteady Reynolds-averaged formulations. The computations produced η values which were considerably higher than the experiments. Holloway et al. [2] suggested that the difference was due to coherent unsteadiness that was not captured by their computation

Most numerical studies of the trailing edge configuration have employed Reynolds averaged (RANS) models (Holloway et al.[2], Medic & Durbin [3], Menter & Egorov [4]). Unsteady RANS shows that coherent vortex shedding from the nozzle lip plays a critical role in the flow around the break out. Figure 2 is an illustration. It shows shedding from the upper nozzle lip. Unfortunately, in all of these studies the natural unsteadiness was unable to reproduce the drop in effectiveness seen in laboratory experiments. In the case computed by Medic & Durbin [3] and by Holloway et al. [2] the observed effectiveness was 0.5, the computed effectiveness was 0.9. An unknown process seemed to be enhancing mixing beyond what could be explained by vortex shedding alone.
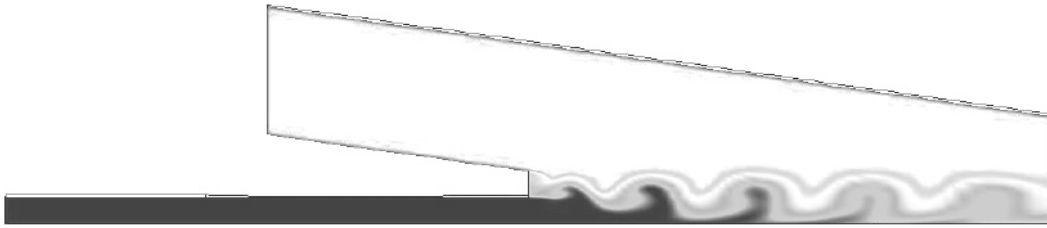
Figure 2: Vortex shedding from upper nozzle lip: temperature contours. From Medic & Durbin [3]

Medic & Durbin [3] found that unsteady RANS could reproduce the observed drop of effectiveness if periodic fluctuations were applied at the film coolant exit. Forcing of the coolant flow caused the shed vortices to develop into vortex loops, as shown in Figure 3. These vortex loops enhanced mixing and decreased η to the levels seen in experiment. Figure 4 shows the resulting film cooling effectiveness along the centerline for the two cases, compared to experiment.
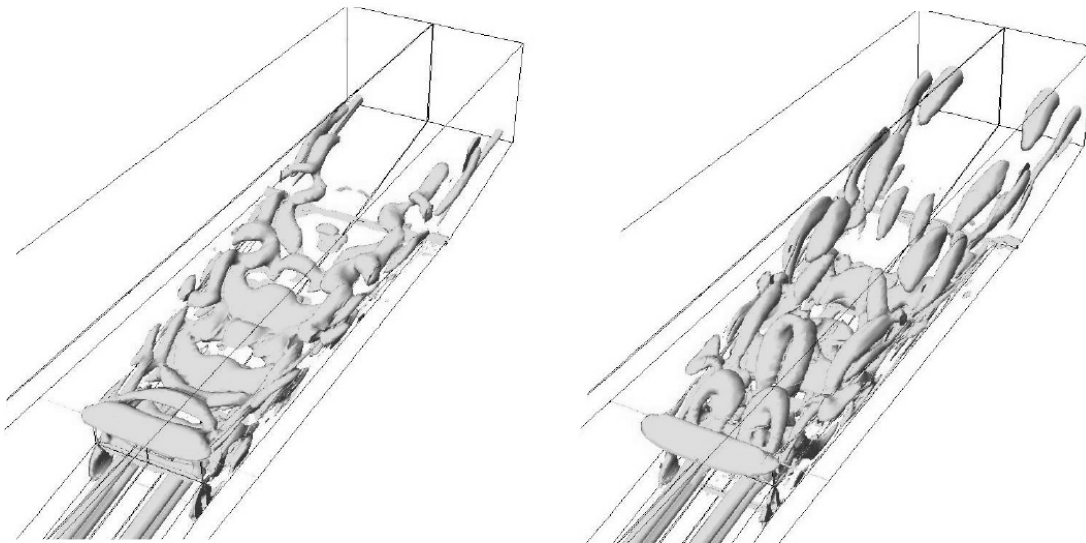

Figure 3: Natural (left) and forced (right) unsteadiness in RANS simulations (Medic & Durbin [3]).
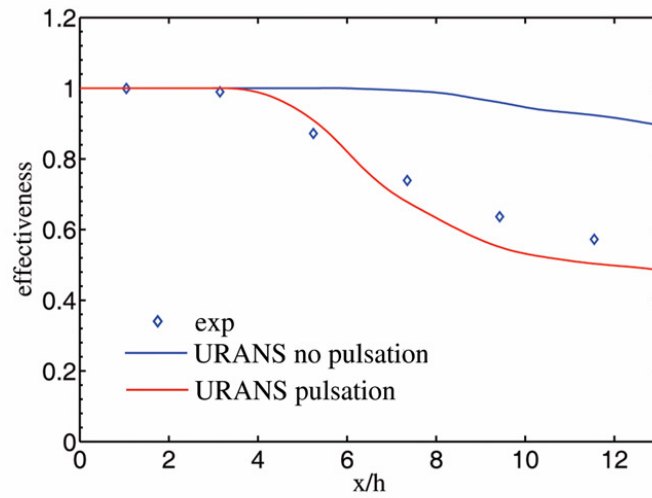
Figure 4: Centerline adiabatic cooling effectiveness for natural and forced unsteadiness in RANS simulations compared to experiment (Medic & Durbin [3]).

These simulations suggest a possible mechanism for the strong mixing present in real trailing edge breakouts. However, the vortex loops were produced by a computational artifice, and it is not known if there is any reason for those coherent vortex loops to form in turbulent flow in this geometry. There are no spatially resolved turbulence measurements around a 3D breakout geometry to compare with the simulations. Uzol and Camci [5] acquired PIV data around the trailing edge of a film-cooled turbine, but only presented the velocity magnitude in a single plane

The goal of the present work is to provide highly resolved turbulence measurements in the immediate vicinity of a realistic trailing edge breakout and new simulation methodologies capable of capturing the mixing structures without arbitrary forcing. Both experiments and simulations are performed for a simple symmetric airfoil rather than a highly cambered turbine airfoil to avoid measurement difficulties associated with a highly curved flow passage. The airfoil is mounted in a converging flow channel in order to obtain an overall favorable pressure gradient similar to turbine flow. Two different experiments are used. The first one uses particle image velocimetry (PIV) in a low speed water flow apparatus. This experiment served to prove the concept and provide early data for comparison to simulations. A second transonic experiment was designed and built to operate at full-scale Mach and Reynolds numbers. The simulation method is Detached Eddy Simulation (DES) using the Scale Adaptive Simulation (SAS) approach developed by Menter & Egorov [4]. The model is implemented in the in-house SUMB code developed under DOE funding. Finally, a new method based on Magnetic Resonance Imaging (MRI) is being developed to measure the three-dimensional coolant concentration distribution in order to assess the accuracy of film-cooling effectiveness simulations.

The low speed experiment and computation are now complete, and the full set of results for both will be presented here. The transonic experiment has been designed, built, and tested, and preliminary measurements are presented here.

2 Computational Approach: Eddy Simulation

Trailing edge film cooling flow is challenging to compute. Eddy simulation promises detailed information which can reveal the complex, and poorly understood, mixing mechanisms that occur in this flow. Menter & Egorov [4] presented a form of eddy simulation which they called scale-adaptive simulation (SAS). Functionally, it involves adding a term that constrains the level of eddy viscosity, and permits chaotic eddying, to the RANS model. Natural instability of separated shear layers is exploited to permit eddies to develop.

One of the illustrations in Menter & Egorov [4] is a trailing edge cooling geometry. That simulation was described only briefly, but it was noted that SAS produced significantly better agreement to experimental data than unsteady RANS. The particular geometry was a breakout without lands. The coherent unsteadiness seen in the present simulations was not present. Experiments without lands show that the tangential jets are highly unsteady, with no clear coherence (Martini et al. [6,7]).

At this point our terminology should be explained. We use 'eddy simulation' as a general term to refer to computations in which the chaotic state of turbulence is being simulated. The primary distinction is from Reynolds averaged simulation. SAS is formulated as a hybrid RANS/LES approach. The eddying region is regarded as a 'large eddy simulation' region — however, the SAS model is not entirely equivalent to LES so it is preferable to refer simply to 'eddy simulation'. As will be seen, the Reynolds number is fairly low in the present simulation, the fully RANS region *per se* is absent, and the simulation is similar to LES.

2.1 Numerical Methods and Models

The simulations made use of the SuMB computational fluid dynamics code as described in Van der Weide et al. [8]. This is a multi-block, structured grid code. It solves the compressible Navier-Stokes equations, discretized into finite volumes. Solution variables are collocated at cell centers. Time accuracy is achieved by dual time-stepping. The true time-step is discretized by second order, backward Euler differencing. Each true time-step is sub-integrated in pseudo-time by the 5 stage, Runge-Kutta scheme of Jameson [9]. Convergence is accelerated by multi-grid iterations. The Runge-Kutta integrations function as a smoother on the successively coarser grids.

SuMB is a fully compressible Navier-Stokes code. The present simulations were nearly incompressible; the reference Mach number was 0.2. The basic equations that SuMB solves are the unsteady, compressible momentum, continuity and energy equations:

$$\frac{\partial \rho U}{\partial t} + \nabla \cdot \rho U U = \nabla \cdot \Sigma$$

$$\frac{\partial \rho}{\partial t} + \nabla \cdot \rho U = 0$$

$$\frac{\partial \rho e_t}{\partial t} + \nabla \cdot (\rho e_t + P)U = \nabla \cdot (\kappa + \kappa_T)\nabla T$$

(2.1)

where the stress tensor is

$$\Sigma_{ij} = -P\delta_{ij} + (\mu + \mu_T)\left(\frac{\partial U_i}{\partial x_j} + \frac{\partial U_j}{\partial x_i}\right) - \frac{2}{3}(\mu + \mu_T)\frac{\partial U_k}{\partial x_k}\delta_{ij}$$

(2.2)

and the total energy is

$$e_t = C_v T + \frac{1}{2}|U|^2$$

(2.3)

C_v is the specific heat capacity. The equation of state $P = \rho RT$ completes the system. The equation for a diffusive, passive scalar is

$$\frac{\partial C}{\partial t} + \nabla \cdot \rho C = \nabla \cdot (\alpha + \alpha_T)\nabla C$$

(2.3)

Equations (2.2) and (2.3) contain eddy transport coefficients, υ_T and α_T. The eddy diffusivity is given by $\alpha_T = \upsilon_T/Pr_T$ with $Pr_T = 0.9$. A turbulence model — in the present case, SST for RANS and SST-SAS for eddy simulation — determines the eddy viscosity throughout the flow field.

A number of modifications to the numerical discretization and time advancement methods were effected for the present application. These were required in order to obtain the accuracy and stability needed for eddy simulation.

2.2 Scale adaptive simulation

The SST RANS model (Menter [10]) is a variant of the $k - \omega$ model. The scale adaptive SST model is the RANS model with an extra term in the ω equation. In SAS, the adaptive scale is provided by the von Karman length (Menter & Egorov [11]):

$$L_{vk}^2 = \frac{|\kappa S|^2}{|\nabla^2 U|^2}.$$

(2.4)

where $\kappa = 0.41$. The denominator denotes $\nabla^2 U_i \nabla^2 U_i$,

$$|S|^2 = 2S_{ij}S_{ji} \quad \text{with} \quad 2S_{ij} = \partial_i U_j + \partial_j U_i \tag{2.5}$$

In parallel shear flow this scale becomes $L_{vk} = |d_y U/d^2_y U|$. If L_{vk} were used in an eddy viscosity transport model, assuming that destruction and production were in balance would give

$$\nu_T \sim L_{vk}^2 |S| \tag{2.6}$$

Thus L_{vk} can be understood to be a bit like a mixing length.

The use of a flow dependent length scale is the *scale adaptive* aspect of the SAS formulation. Although Menter & Egorov [11] argued that L_{vk} was a natural flow scale, as opposed to the grid scale Δ, when it is evaluated by finite differences on a typical SAS grid, L_{vk} varies in approximate proportion to Δ — indeed, it draws a connection to LES subgrid models.

In order to ensure that the model dissipates small scales, the eddy viscosity is prevented from dropping below the level of the Smagorinsky subgrid model. A limiter is applied to redefine the von Karman length as

$$L_{vk} = \max\left[\frac{\kappa|S|}{|\nabla^2 U|}, \frac{0.358 C_\mu \Delta}{\beta - C_\mu \alpha}\right] \tag{2.7}$$

where $C_\mu = 0.09$ and $\beta = 3/40$ in the $k - \omega$ model (it is interpolated between this and 0.0828 in the SST model).

The SST-SAS model was originally derived from an eddy viscosity transport equation by adjoining the k-equation to it. Then it was converted to a pair of equations for k and ω. The outcome is to add the term

$$Q_{SAS} = \rho \max\left\{2.65 \frac{L}{L_{vk}}|S|^2 - 6k \max\left[\frac{|\nabla\omega|^2}{\omega^2}, \frac{|\nabla k|^2}{k^2}\right], 0\right\} \tag{2.8}$$

to the ω equation, where

$$L = \frac{\sqrt{k}}{C_\mu^{1/4}\omega}$$

Constants given in Menter et al. [12] have been substituted to obtain the numerical value 2.65 in (2.8). The *max* functions in (2.8) help to preserve the RANS behavior near walls.

2.3 Treatment of convection

Eddy simulation requires low dissipation convection schemes. The native discretizations in SuMB are unsatisfactory for present purposes. Alterations were made to the treatment of convection. Initially a centered discretization was tried for convective flux interpolation. That proved to be unstable. A skew symmetric convective form was found to be stable and accurate. The compressible, skew form for the flux derivative is

$$\frac{\partial \rho u_i u_j}{\partial x_j} = \frac{1}{2}\left[\frac{\partial \rho u_i u_j}{\partial x_j} + \rho u_j \frac{\partial u_i}{\partial x_j} + u_i \frac{\partial \rho u_j}{\partial x_j}\right]$$

(2.9)

The rationales given in the literature for this form are consistency with kinetic energy conservation, via the discrete product rule, and reduction in aliasing error. A finite volume discretization of (2.9) was implemented into the simulation code. Fluxes on the centers of cell faces are approximated by the average of cell-center values. The terms that are not in conservation form are obtained from cell face values times derivatives obtained by Gauss' theorem. In short, standard, second order, centered formulas are used.

The skew form (2.9) was adopted for both the momentum and the energy equations. Transported scalars are especially prone to numerical oscillations. It has become common practice in eddy simulation to invoke some degree of upwinding to obtain smooth scalar fields. The second order, upwind method of Barth & Jespersen [13] was selected. It invokes a limiter to minimize numerical diffusion; thus, on a smooth field it relaxes to second order central differencing.

The scalar flux $C \equiv \int \nabla \cdot (\rho \phi u) dV$ is expressed as a difference between face centered values. For instance, in the x_i direction

$$C = (\rho \phi u \cdot A)_{i+1/2,j} - (\rho \phi u \cdot A)_{i-1/2,j}$$

(2.10)

The velocity is interpolated to the cell face. The face-center scalar is evaluated by a limited, linear interpolation:

$$\phi_{i+1/2} = \begin{cases} \phi_i & + & \Phi \nabla \phi_i \cdot \Delta S & \text{if } u > 0 \\ \phi_{i+1} & + & \Phi \nabla \phi_{i+1} \cdot \Delta S & \text{if } u < 0 \end{cases}$$

(2.11)

where ∇S is a vector from the upstream cell center (i or $i+1$) to the center of the face ($i+\frac{1}{2}$). The gradients, $\nabla \phi_i$, are computed by Gauss' theorem. The coefficient Φ is a limiter that satisfies $0 \leq \Phi \leq 1$. It introduces upwind biasing. The limiting scheme is described in Barth & Jespersen [13].

2.4 Implicit Compact Filtering

A very weak numerical instability was observed as simulations proceeded. As it was of high spatial frequency, a low pass filter was applied periodically to suppress it. A compact, Padé type of formulation was used. The filtering scheme is

$$\alpha \hat{f}_{i+1} + \hat{f}_i + \alpha \hat{f}_{i-1} = a f_i + \frac{1}{2}b(f_{i+1} + f_{i-1}) + \frac{1}{2}c(f_{i+2} + f_{i-2})$$

(2.12)

where

$$a = \frac{1}{8}(6\alpha + 5), \quad b = \frac{1}{2}(2\alpha + 1), \quad c = \frac{1}{8}(2\alpha - 1) \alpha = 0.475$$

This is applied separately along each computational coordinate. $\hat{f}$ is the filtered value of a variable and f is the value before filtering. Near boundaries the full stencil is not available. At such locations the explicit filter

$$\hat{f}_1 = \frac{15f_1 + 4f_2 - 6f_3 + 4f_4 - f_5}{16}$$

was applied. The filtering operation is to replace all field variables, f, by their filtered values, $\hat{f}$. The filter is designed to be flat at low wavenumber and to cut off at high wavenumber. It will be seen that the cutoff is well above frequencies of present concern.

2.5 Inflow conditions

In order to inject a turbulent inflow, the entrance to the computational domain was treated as an interface between two flow fields, rather than an inlet, per se. In particular, the usual characteristic inflow conditions would permit 4 quantities to be given and the fifth would be extrapolated from the interior. However, at an interface between computational blocks, all 5 variables are prescribed from an adjacent block. On the inlet plane, all three components of **u**, the pressure, p, and density ρ are prescribed as a function of position at each time.

It proved necessary to include eddies at the inflow in order to stimulate turbulent motion in the separation region. To this end, inflow data were generated by a separate large eddy simulation of a turbulent boundary — the LES code was provided by Kang & Choi [14]. The rescaling and recycling technique of Lund et al. [15] was used to create a fully developed boundary layer.

While the LES simulation provides a full velocity field, quantities such as k and ω also are needed for the SST-SAS model. In the SAS mode, k and ε can be understood as

subgrid scale residual kinetic energy and dissipation. Although more sophisticated methods could be investigated, currently a rather straightforward approach was used. Assuming that the LES field resolves almost all turbulent kinetic energy, a box filter was applied over the field. The filter width was small enough to preserve most of the energy. The residual kinetic energy was defined as

$$k = \frac{1}{2}U_i U_i - \frac{1}{2}\hat{U}_i \hat{U}_i$$

ε was estimated from subgrid scale dissipation as

$$\epsilon \approx 2\nu_{T,SGS} S_{ij} S_{ij}$$

Finally ω was evaluated as ω = ε/(0.09k).

2.6 Flow configuration

The calculations were performed for the geometry and conditions used in the subsonic experiment. The computational domain is portrayed at the left of Figure 5. The inflows above and below the blade are labeled as 'interfaces' because data from a large eddy simulation are provided there. At the coolant inflow, the bulk velocity is specified: it is unity by the present non-dimensionalization. The lateral boundary conditions are periodic, emulating a row of cooling slots along a trailing edge.
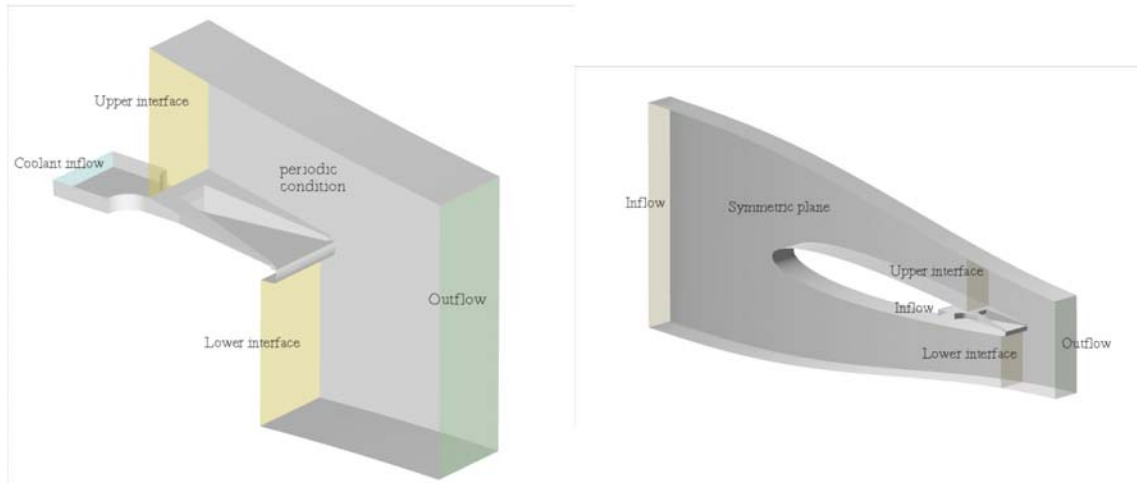

Figure 5: Schematic of the eddy simulation setup and of the whole channel RANS simulation setup.

The eddy simulation was preceded by a RANS computation on the domain shown at the right of Figure 5. This contains a whole blade in a domain that was designed to emulate the pressure field of a turbine stage. The RANS simulation provided a mean flow at the inlet to the eddy simulation. This procedure is illustrated by Figure 6. Data are extracted

from the RANS computation, then boundary layer turbulence is added (as described in §2.5) to generate an inflow for the eddy simulation.
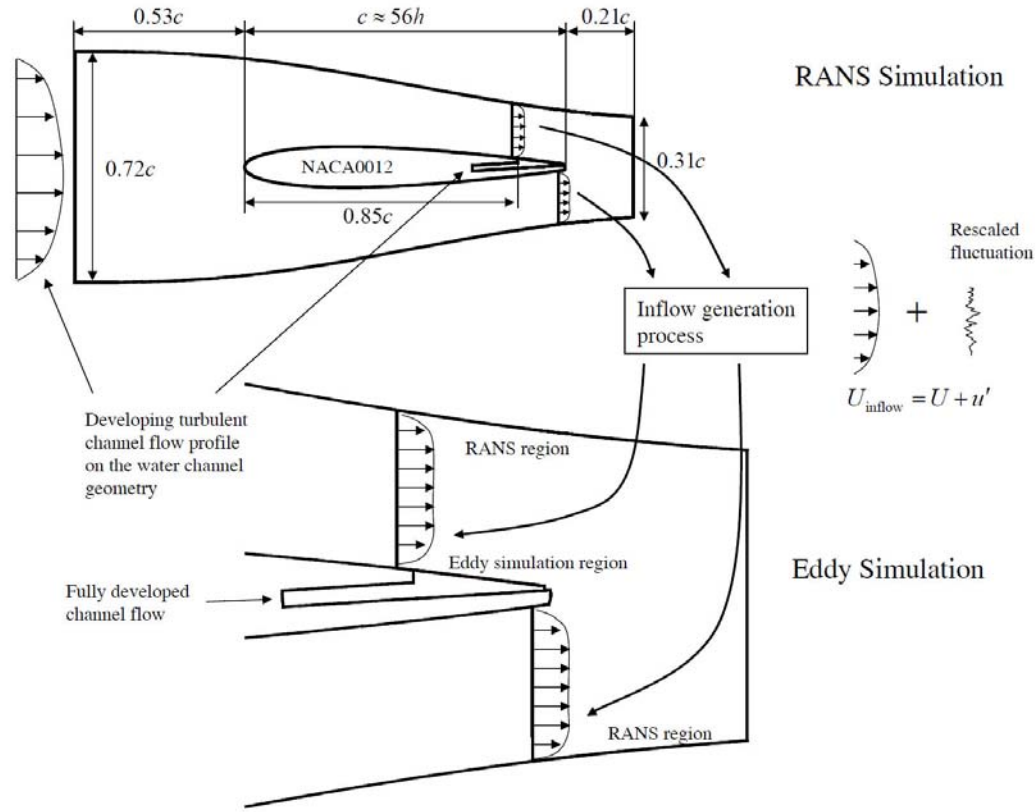

Figure 6: Schematic of the procedure of the trailing edge simulation.

The grid sections in Figure 7 give an overview of how the full domain was meshed for the eddy simulation. The computational domain extends inside the blade, starting in a plenum. Above the blade the grid becomes coarse in the free-stream. This is a structured, multi-block grid; the total number of computational blocks is 54.

Lengths are non-dimensionalized by the slot height, h, and velocities by the bulk velocity of the *cooling jet*, U_0. In these units, the nozzle lip thickness is 0.7. The surface between the lands slopes at about 3° from the horizontal, so the wall is at a distance 0.05x above the x axis. The origin is at the center of the breakout. The trailing edge is 8.3 slot heights from the breakout. The width of the breakout is 5. The overall domain width is 12: periodic boundary conditions make this the repeat unit of a periodic array of trailing edge cooling slots. The Reynolds number based on the height and the bulk velocity of the channel is 7,385. This is representative of the trailing edge slot Reynolds numbers of high pressure turbine blades.
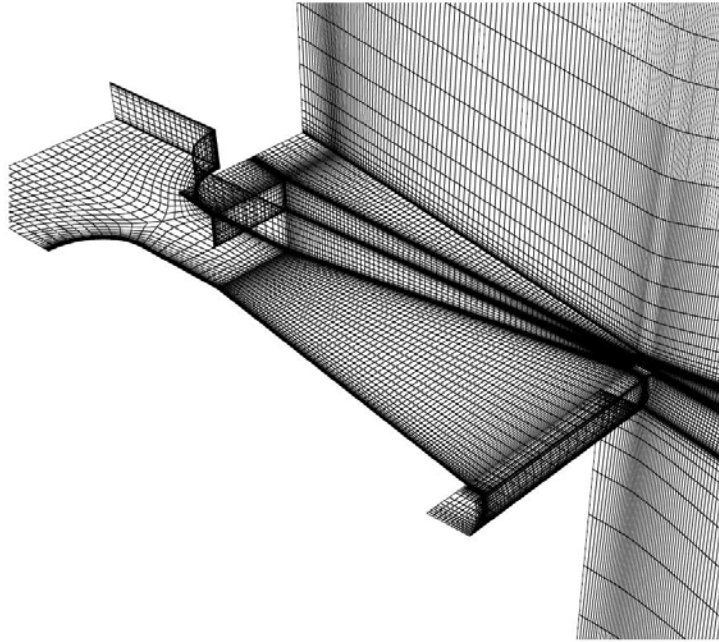
Figure 7: Sections of the grid for the trailing edge and coolant passage.

A time step of 0.0257 was used for the blowing ratio 1 case. For the blowing ratio of 1.5 case, the time step was reduced to 0.0185, due to the increased jet Reynolds number. To assess the temporal resolution, two different time steps, of 0.0514 (in units of h/U_0) and 0.0257, were tested. With the larger time step, turbulent fluctuations were somewhat damped. The well resolved energy spectra (shown in section X) indicates that the current temporal resolution is sufficient.

Before collecting statistics, simulations were run for 10 flow-through times. Then statistics were collected over 13.8 flow-through times. The compact filter (§2.4) was applied once every 47 time steps to remove grid-wise oscillation.

Unsteady RANS simulations were also done in the trailing edge geometry. The time step size was 0.063, which resolves one shedding period into 66 time steps. 9 flow through times were allowed for initial transients. After that, the periodic, Reynolds averaged state was reached.

Extensive grid refinement and validation studies are presented in Joo [16]. Under the scale adaptive modeling approach, the greatest concern is to resolve the separated region. In a preliminary study, very coarse grids with high stretching ratios were tested. Severe grid-to-grid point oscillations and spurious, streamwise waves in the vorticity field were observed. As a result of this preliminary study, a grid was created with 8 million computational cells. The final grid was created by refining this in each of the x, y and z directions. Overall comparisons between the 8 million point grid and final grid resolutions are summarized in tables 1 and 2. Comparisons are illustrated by Figure 8: a

good number of similar comparisons were made by Joo (2008). Overall, the base and fine cases are in good agreement, indicating that the final grid provides sufficient resolution.

case	grid size of near the slot region	total nunber of computational cells
base	200x100x80	8.04×10^6
final	224x152x128	20.0×10^6

Table 1: Grid refinement for the eddy simulations.

case	base	final
Δy^+_{min} at x=0	0.8	0.8
Δy^+_{max}	43.62	24.1
Δx^+_{min}	7.2	7.2
Δx^+_{max}	33.4	27.65
Δz^+_{min}	1.6	1.6
Δz^+_{max}	59.5	32.5

Table 2: Maximum and minimum grid sizes in the slot region of the eddy simulations.
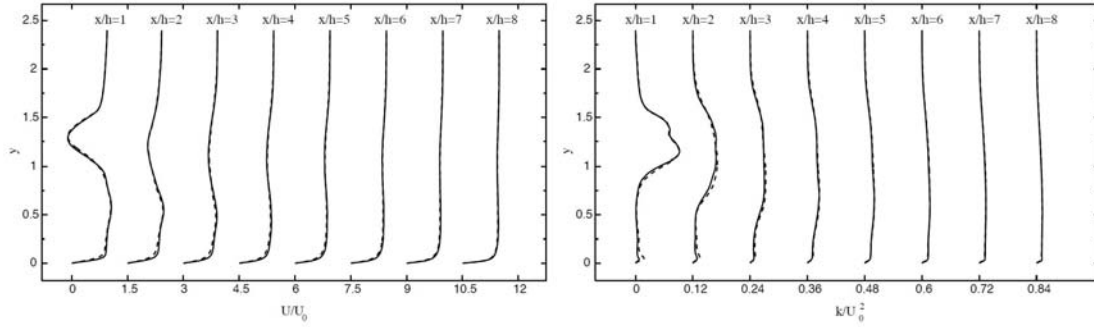
Figure 8: Comparison of mean velocity and turbulent kinetic energy profiles between the base and final grids. : final grid; : the base grid.

3 Experiment 1: Subsonic Flow

The subsonic experiment was designed to test the flow configuration prior to implementation in the transonic facility, and to provide early data for comparison to the

simulations. The pilot experiment uses a symmetric airfoil in a water tunnel with a 2D contraction designed using CFD to approximate the acceleration seen in the turbine. The airfoil is a NACA 0012 equipped with trailing edge breakout slots that mimic those found in a modern high pressure turbine, as shown in Figure 1. The experiment is run at low speed with a Reynolds number of 78,000 based on the blade chord. PIV measurements were obtained around the trailing edge breakout geometry, providing two components of mean velocity and turbulence at three spanwise positions. These measurements were used as a proof-of-concept and they were used to guide the design of the full-scale transonic experiment.

3.1 Experimental apparatus

Figure 2 shows a schematic of the apparatus for the subsonic experiments. Measurements were acquired in the trailing edge region of the symmetric airfoil modified to include a realistic trailing edge breakout. Figure 9 shows an overall schematic of the experimental apparatus. The airfoil was mounted in a small recirculating water channel. Two contraction inserts were placed inside the channel to accelerate the flow near the trailing edge to mimic the overall favorable pressure gradient in a turbine stage. All measurements were acquired using 2D PIV focusing on the trailing edge region.
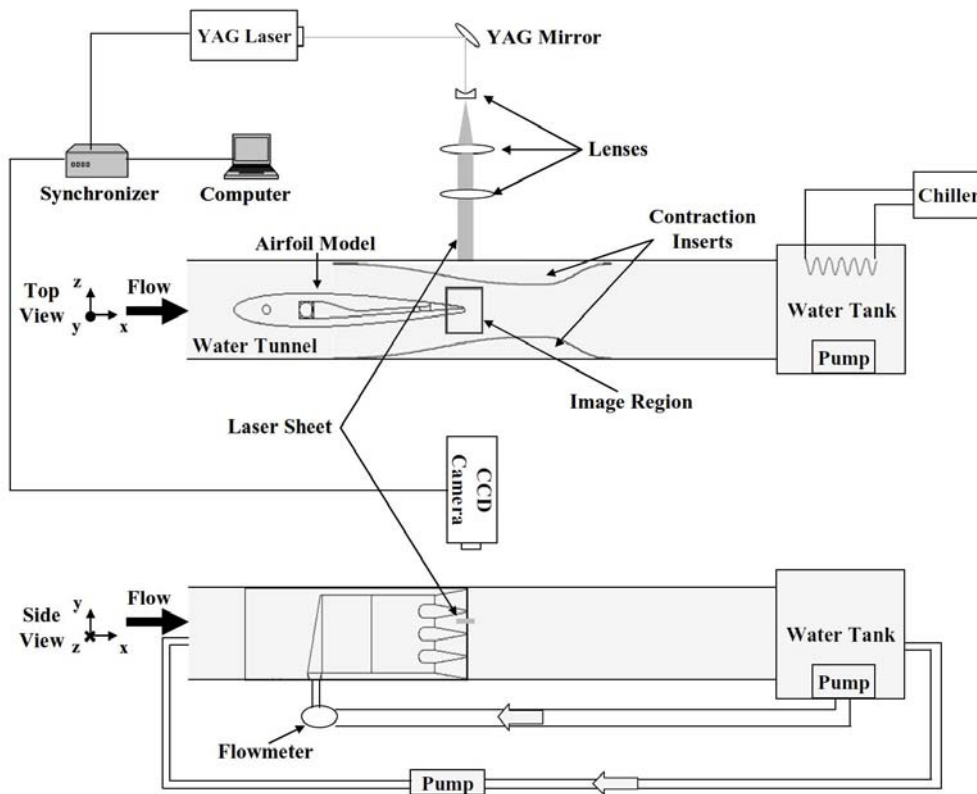

Figure 9: Schematic of experimental setup

3.2 Airfoil model

The base airfoil is a conventional NACA 0012 airfoil with a nominal chord length (*c*) of 150 mm and a total span of 49 mm. The last 5.7% of the chord length was removed to create a blunt trailing edge and an actual chord length of 141.5 mm. The breakout geometry is the same as the one used for the simulations, as shown in Figure 1 above. It occupies the final 21 mm (14%) of the chord. There are four coolant exits each with a 5 mm x 2.5 mm rectangular shape, with a 1.9 mm lip thickness. These slots are separated by trapezoidal lands. The lands are 7 mm wide at the breakout, and are protruded downstream until 0.87 mm before the trailing edge, ending with 1 mm width and 0.71 mm thickness. All parameters in the breakout region were chosen based on approximate measurements of several modern turbine blades.

Film cooling flow is supplied through one end of the airfoil into a triangular manifold as illustrated in Figure 10. This manifold feeds a 3.6:1 two-dimensional contraction which passes into a 41 mm x 2.5 mm x 30 mm long rectangular channel. Flow divides into four supply channels with semicircular leading edges. The flow dividers protrude 10 mm upstream of the breakout to allow the flow to pass smoothly out of the breakout slots.

The model was fabricated in Waterclear resin using a 3D Systems Viper stereolithography system (SLA) operated at maximum resolution (0.013 mm/layer). This resin produced a model which was transparent when immersed in water allowing the PIV laser sheet to pass through with minimum attenuation. Figure 11 shows the complete airfoil model. A hole near the leading edge was used to mount the model in the water channel, and a hole around the quarter-chord was used to supply the cooling flow.
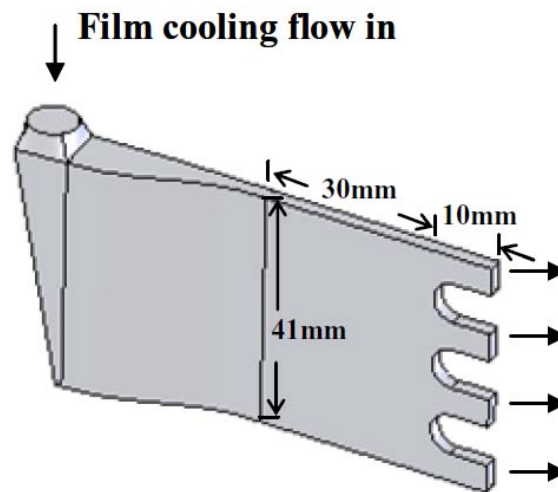

Figure 10: Film cooling supply channel

Figure 11: SLA airfoil model

3.3 Overall water tunnel system

We installed the airfoil model in a 51 mm x 102 mm rectangular cross section water tunnel with a gasket filling out the gaps (Figure 9). It was mounted midway along the 1 m long test section. The recirculating water channel is driven by a 0.37 kW centrifugal pump. This feeds an entrance section including a diffuser, three grids and two honeycomb sections to achieve uniform flow. The water tunnel is made of Plexiglas, with two glass viewing windows located on the top of the channel for CCD camera access and on the side for the laser sheet. Flow discharges from the test section into a water reservoir. A heat exchanger coil attached to a chiller unit was mounted in the reservoir and was set to maintain the water temperature at approximately 22 °C.

Transparent inserts, which were specifically designed using CFD to form a contraction near the trailing edge were mounted in the test section surrounding the airfoil and extending downstream. The contractions reduce the tunnel area by a factor of 2 with the minimum area located 42 mm downstream of the trailing edge. This produces the desired favorable pressure gradient over the airfoil surface. The mean velocity field for the design calculation is shown in Figure 12 below.
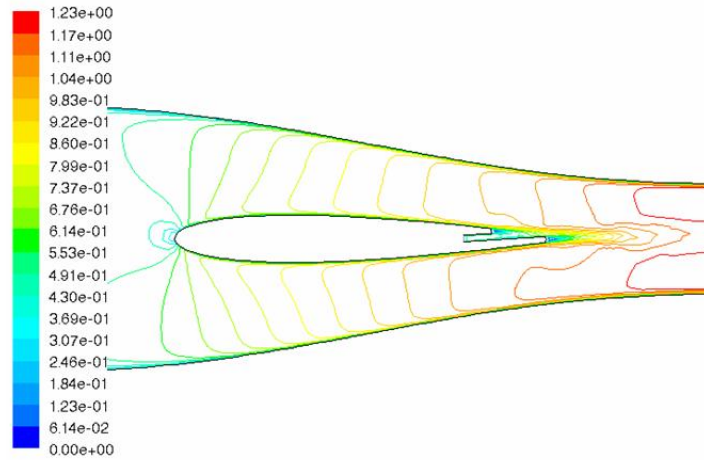
Figure 12: Design calculation for subsonic experiment (mean velocity, m/s)

Film cooling flow was supplied by a second pump (Little Giant MOD 4E- 34NR), immersed in the water reservoir. A Dwyer 2 GPM rotameter-type flowmeter with a built in valve was used to control the film-cooling flow rate. The uncertainty in this measurement was ±0.074 GPM.

The water tunnel was operated at a nominal Reynolds number of approximately 56,000 based on the airfoil chord and the bulk average velocity in the upstream channel. This upstream velocity was calculated using velocity measurements 10 mm downstream of the trailing edge and conservation of mass.

3.4 PIV system

A 2D PIV system with a 50mJ New Wave dual-head YAG PIV laser (wavelength: 532 nm) was used. Sheet forming optics consisting of a 300 mm cylindrical lens, and two spherical lenses produced a sheet approximately 0.5 mm thick by 20.6 mm wide at the trailing edge. The laser sheet passed through the transparent airfoil model providing simultaneous measurements on the upper and lower surfaces. Image pairs were acquired with a 600 μs time delay using a TSI PIVCAM 13-8 with 1,280 x 1,024 pixels resolution with a TSI synchronizer (Model 610034) and TSI Insight software. We collected high resolution image sets in the immediate vicinity of the breakout and in the near wake region at three different spanwise positions.

Image pairs were post-processed using PIVLab software, which was developed at Stanford University (Han 2001) to obtain the velocity vector field. This software uses an iterative cross-correlation technique to calculate the velocity from the particle displacement recorded in each image pair. The final interrogation window size was 32 x 32 pixels with 50% overlap. 1000 image pairs were acquired at each plane at 1 second intervals. The time interval between successive images of a pair was 600 μs. Calibration

was performed to relate particle displacement in the image to the physical displacement by placing a calibration grid with a grid size of 1 mm at the plane illuminated by the laser sheet. The magnification factor was approximately 0.02 mm/pixel.

The uncertainty in the PIV velocity measurements was estimated taking into account the uncertainty in the sub-pixel displacement estimator of ±0.2 pixels, and the uncertainty in the laser sheet alignment of ±1°. The statistical uncertainty of 0.028 m/s near the turbulent region was much larger as opposed to 0.0034 m/s outside the turbulent region. Other uncertainty sources including those due to timing, particle lag, seeding uniformity, and calibration grid accuracy were minor. The total uncertainty calculated at 95% confidence level was ±0.048 m/s near the turbulent region, and ±0.039 m/s away from the turbulent region.

4   Experiment 2: Transonic Flow

The transonic experiment was built based on the geometry of the low speed pilot experiment, with some modifications based on the results of the low speed experiment. The external wall shape around the wing had to be redesigned to account for compressibility effects. The wing and breakout geometry used were the same, with the exception that an additional slot was added to make the spanwise slot array symmetric about the slot centerline. This changed the aspect ratio of the wing, from 0.33 to 0.41. The experimental apparatus was designed around the wing and wall geometry for optimal optical access for PIV measurements, and the rig was installed at our existing transonic cascade facility.

4.1 External geometry design

To duplicate the overall pressure gradient of a full-scale transonic turbine cascade, our initial design goal was to obtain Mach numbers of 0.3 and 0.85 at the wing leading and trailing edges, respectively. This proved difficult with a symmetric passage around the wing, since flow at high Mach number is very sensitive to small changes in area. From a Mach number of 0.85, only a 2% reduction in area is required choke the flow, meaning the minimum cross-stream area would need to be very close to the trailing edge to get M 0.85 at the trailing edge. However it would not be possible to put the minimum area right at the trailing edge without introducing a sharp corner in the wall shape, due to the slope and curvature of the wing trailing edge. Since other sources of error could easily cause the flow to choke in this case (manufacturing tolerances, endwall boundary layers, and effective area loss due to coolant flow), we opted to hold the *exit* Mach number fixed at 0.85, and then inverse-design the rest of the wall shape around the wing for a smooth gradient and high Mach number at the trailing edge.

The design procedure used for the outer wall shape was as follows:

The goal was to produce the desired overall pressure change along the wing, with minimal changes to the subsonic experiment shape. The aspect ratio of the wing was fixed as described above, and again this would be placed in a 2D passage. The nondimensional height of the inlet (before the contraction) and distance from the contraction start to the leading edge were held fixed. The Mach number at the leading edge was set at 0.3. The minimum area was set at the exit, and the exit Mach number was held fixed at 0.85. The unknowns then were the distance from the trailing edge to the exit, and the shape of the wall itself between the fixed endpoints. Projected 1-D area relations were used to determine the wall shape, with a few design iterations checked with CFD to determine the minimum allowable distance from the trailing edge to the exit. The wall shape was designed using the isentropic Mach-number pressure relation:

$$\frac{P_{Tt}}{P} = \left(1 + \frac{\gamma - 1}{2} M^2\right)^{\frac{\gamma}{\gamma - 1}}$$

(4.1)

and the isentropic area-Mach number function:

$$f(M) = \frac{A^*}{A} = \left(\frac{\gamma + 1}{2}\right)^{\frac{\gamma + 1}{2(\gamma - 1)}} \frac{M}{\left(1 + \frac{\gamma - 1}{2} M^2\right)^{\frac{\gamma + 1}{2(\gamma - 1)}}}.$$

(4.2)

A fifth-order polynomial was fit to the Mach number using the geometric constraints above (M=0.3 and 0.8 at leading edge and exit, fixed locations for inlet and exit relative to the leading and trailing edges). Note that for the subsonic wall, 5th-order polynomials were used to describe the wall shape itself. If the same area distribution were used here, the Mach number would be less than 0.6 at the trailing edge, even with M=1 at the exit. Here instead the desired Mach number distribution was specified, and equation 4.2 was then used to determine the area distribution. From there, it would be possible to produce the wall shape from the 1D area distribution simply by subtracting the wing area, but this would not produce the correct pressure distribution because the flow around the wing has a significant vertical component. In addition, splines would be needed at the wing leading and trailing edges to avoid sharp corners and separation along the outer wall.

As a first approximation to compensate for two-dimensional effects, the 1D isentropic area distribution was simply projected out perpendicular from the wing surface. Cubic splines were then fitted at the inlet and exit to adjust the inner geometry to the fixed inlet and exit areas. A few designs were tested using CFD for different spline endpoint positions, and these results suggested the projected-area approach would be sufficient to achieve the desired pressure distribution. The final geometry and expected Mach number distributions are shown in Figures 13 and 14 below.
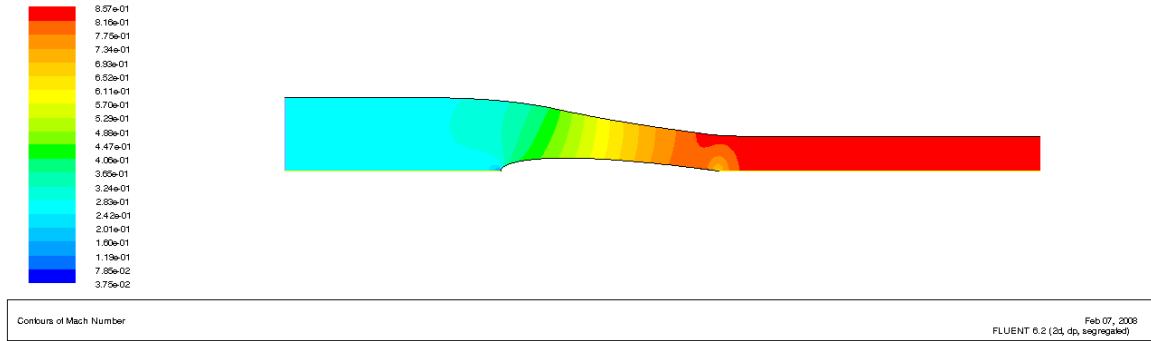
Figure 13: Predicted Mach number contours for 2D wall geometry (inviscid calculation, simple wing without breakouts)
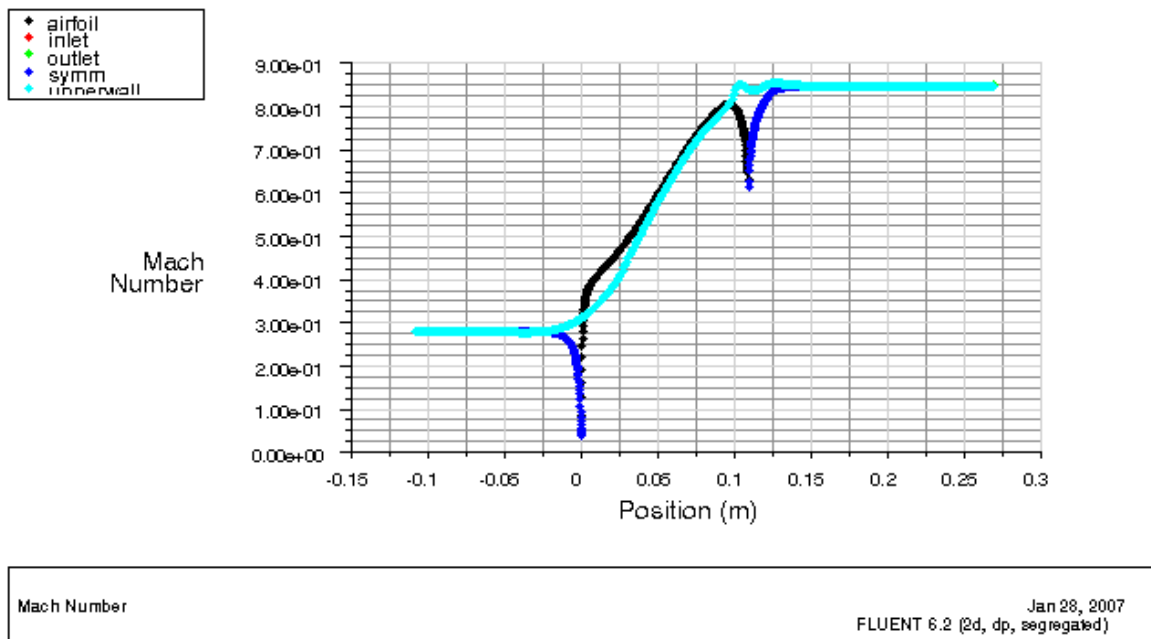
Figure 14: Predicted Mach number distribution along wing and wall surfaces for 2D wall geometry

4.2 Optical design

Once the inside wall shape was determined, the outer wall shape was then inverse-designed to act as a lens for the PIV laser light sheet. The approach used was the same as that used for the double passage experiment, as described in [17]. The problem was particularly challenging since we wanted to build one set of walls that would account for different angles. The final wall shape allows light to pass through the walls undisturbed from three angles. This result is summarized in Figure 15.
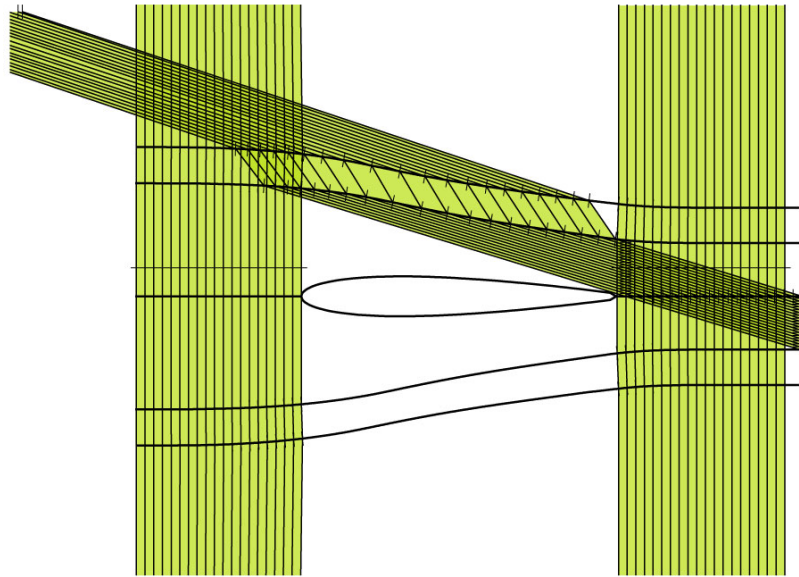
Figure 15: Wall shape design using ray-tracing technique

4.3 Overall wind tunnel design

Given the set inside and outside geometry, 3D wing geometry, and aspect ratio, the overall scale was determined based on the mass flow available from our compressor, The resulting wing chord is 117 mm, the span is 47.5 mm, and the inlet and exit heights are 39.7 and 18.7 mm respectively. The rest of the wind tunnel was designed around the geometry to adapt it to our steady-flow, transonic wind tunnel used previously in this program, while maximizing optical access to the wing for PIV measurements. The two-dimensional passage is formed between two parallel aluminum plates in the plane of the figure with a spacing of approximately 1 chord length. The passage walls were CNC machined out of transparent acrylic to the prescribed internal and external shape. To seal the connection between the walls and the aluminum end plates a 1.6 mm O-ring groove was cut parallel to the inner wall surface on both sides of each plastic part. Steel alignment pins were press-fit into the sides of each part, and they mate with matching holes in the aluminum endwalls to lock the walls in the correct location with respect to the central blade. The transparent passage walls are clamped between the two end plates with a set of bolts running in the spanwise direction.

The wing was manufactured using stereolithography (SLA), as for the subsonic experiment. Since the subsonic experiment showed some asymmetry in the flow for the zero-blowing ratio case, for the transonic experiment a wing without any breakout geometry was also built to serve as a baseline for comparison of the measurements. Both wings fit interchangeably into an EDM-cut slot in one of the aluminum endwalls, and

they included gasketed flanges that bolt onto the outside of the endwall. The opposite endwall includes two windows for PIV imaging. The two 12.7 mm thick optical-quality glass windows fit into machined pockets flush with the endwall surface. The window joints are sealed with O-rings which also serve to lock the windows in place between the passage walls and the aluminum end plates. On the window side of the inside passage the wing sits flush with the glass, where it is sealed with a laser-cut Teflon gasket (.005" thick) and vacuum grease. A screw threads through a hole in the endwall between the two glass windows into the wing to reinforce the seal at the wing-window interface. O-rings provide sealing at all flange connections. The flanges at each end were split into four separate parts with alignment pins, to allow for the endwalls and side walls to be removed independently for cleaning and for image calibration.

The wing without slots was equipped with 19 static pressure taps, while the slotted wing had 17 taps along the surface and three taps inside the supply flow plenum. Holes with a diameter of 0.58 mm were drilled perpendicular to the blade surface mid-span and were connected to a Scanivalve (model SSS-48C-MK4) through vinyl tubes extending out the far endwall. The pressure was measured relative to the flow stagnation pressure at the inlet using a Kiel probe and a Setra model 204D pressure transducer. Voltage signals were acquired using a National Instruments PC-MIO-16E-4 board and controlled using LabVIEW software. The resulting pressure measurements were then used to calculate the wing surface isentropic Mach number distribution using equation 4.1.

4.4 Overall Wind Tunnel System

Flow is provided by an Ingersoll-Rand compressor (SSR-XF400), which provides a continuous flow of 0.64 kg/sec at 5.7 x 10^5 Pa. Upstream of the test section the flow passes through an air filter (F18-C00-A3DA) followed by a regulator (Norgren R18-C05-RNSA) which is used to control the total pressure in the test section. After the regulator, the flow passes through a heat exchanger (CMS Heat Transfer Division, Inc.) which uses a variable supply of chilled water to keep the test section temperature constant at 295 K. Following the heat exchanger the flow passes through a corner-flange orifice plate. The mass flow rate is determined from the pressure drop across the orifice plate.

The flow develops in a 1.5 m long duct with an 115 by 86.4 mm cross section. This development duct includes three honeycomb sections (51 mm long by 6 mm cell size) as well as six 1.6 mm thick circular-hole grids (47% - 52% blockage) to produce uniform flow at the entrance to the contraction. The three-dimensional nozzle at the entrance to the test section has a 2.6:1 area contraction ratio reducing the passage size to the 79.4 by 47.5 mm dimensions of the test section inlet. Wall contours in both contracting directions were designed using 5th order polynomials with zero first and second derivatives at the inlet and outlet to insure thin boundary layers at the test section inlet. A removable grid could be installed just upstream of the contraction. This grid produced freestream turbulence levels in excess of 14% upstream of the contraction. The contraction reduced the turbulence intensity to approximately 5-10% at the test section inlet. After passing through the test section, the flow exhausts into a plenum chamber, which is adapted to a

muffler that exhausts to atmosphere.

The total pressure in the test section was measured with a Kiel probe positioned at midspan 28.6 mm downstream of the passage inlet, and was monitored for the duration of each experiment using a Bourdon tube manometer (Wallace & Tiernan FA 145) and a Setra 204D (0-5.7 x 10^5 Pa) pressure transducer. The temperature was measured upstream of the contraction using an Omega 44004 thermistor.

For the trailing edge breakout flow, a second air supply system was constructed that operates independently of the main flow. A second compressor provides the flow, with a regulator used for control. A Laminar Flow Element (Meriam) was used to set the desired blowing ratio at the breakout slots. Two transducers measure the absolute pressure and the pressure drop across the LFE to determine the mass flow rate. The laminar flow element is connected with a straight PVC pipe section, which is then connected to the supply hole in the wing (Figure 10) via a hose.

4.5 PIV Setup

The mean velocity and turbulence quantities were measured using two-dimensional digital particle image velocimetry (PIV). The tracer particles are condensed oil droplets provided by the screw-type compressor, and they are less than 1 μm in diameter as described in [17].

A double pulsed Nd:Yag laser (New Wave Gemini) was used to illuminate the tracer droplets.   The laser generates a maximum energy of about 200 mJ per pulse at a wavelength of 532 nm. Two mirrors were used to direct the beam to the laser sheet optics, which consist of a cylindrical lens and a spherical lens with focal lengths of –50 mm and 500 mm respectively. The resulting light sheet had a thickness of approximately 120 μm at the waist. The optics were positioned for each measurement set so that the sheet enters the passage through the acrylic sidewall at midspan, parallel to the passage geometry, with the sheet waist at the region of interest in the passage.

Images were acquired using a LaVision camera (FlowMaster) and LaVision frame grabber. The camera was used with a Nikkor 200 mm lens at f/4 and was oriented perpendicular to the light sheet.   Timing signals for the laser pulsing and camera exposure were controlled with a LaVision synchronizer and LaVision DaVis software. A macro was used to export the images in tiff format continuously during the data acquisition. Image pairs were acquired at a nominal rate of 1 Hz.

PIV measurements were calibrated using a black-anodized aluminum plate etched with the test section geometry and a superimposed grid. A calibration image was obtained for each measurement set by removing the test section from the wind tunnel and positioning the calibration plate in the spanwise location of the light sheet. This image was used to determine the magnification of the imaging system and the location of each measurement window. The aluminum endwall with the glass windows was left in place while the rest

of the wind tunnel was removed for the imaging. A similar calibration plate was also constructed to position the light sheet in the correct spanwise position. This turned out to be necessary due to the high spanwise velocity gradient. The distance between measurement sets in the spanwise direction is approximately 2 mm. The PIV images were processed using PIVlab software, which uses an iterative technique as described in section 3.4.

5   Results – Detached Eddy Simulation

5.1 Mean velocity and turbulence

An overview of the simulation is provided by Figure 16. This consists of three copies of the exterior flow domain, to create an impression of the trailing edge geometry. The contours are surfaces of constant Q, where $Q \equiv |S|^2 - |\Omega^2|$. The Q iso-surfaces give an impression of eddies forming in the detached shear layers over the cooling slot.
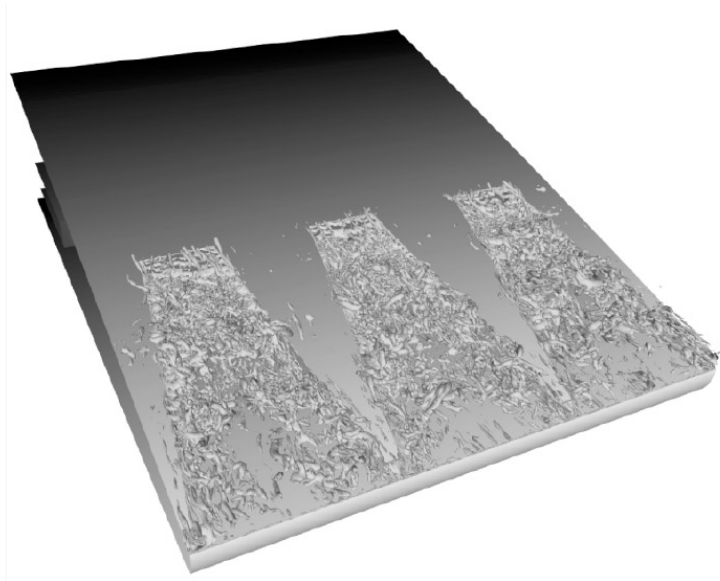
Figure 16: Q iso-surface of eddy simulation with br=1

Mean flow profiles at the two blowing ratios of br = 1 and br = 1.5 are provided in Figure 17. These are shown at mid-span (z = 0). The wake of the upper nozzle lip is visible at x = 1. By x = 3 the profile has developed into a wall jet in a coflowing stream. For the case of br = 1 the bulk velocity of the jet matches that of the free-stream and the profile develops the appearance of an accelerated boundary layer. For br = 1.5 the character of a wall jet in co-flow is present to the trailing edge. A RANS computation with br = 1 is included in Figure 17 for comparison. The eddy simulation and RANS profiles are quite similar.
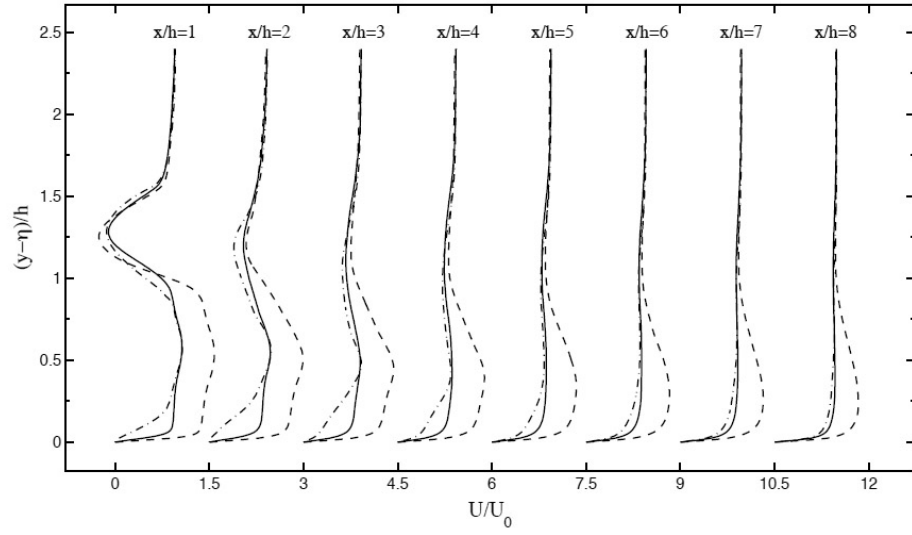
Figure 17: Mean velocity profiles in planes of constant z. solid line: eddy simulation with br=1; dashed line: eddy simulation with br=1.5; dash dot: RANS with br=1

At x = 1, the profiles of resolved turbulent intensity in Figure 18 show a local maximum in the wake of the upper nozzle lip. The maximum is most pronounced for the case with br = 1.5. The profiles spread into the slot with downstream distance. Turbulent intensity levels are similar to those seen in wall jets.
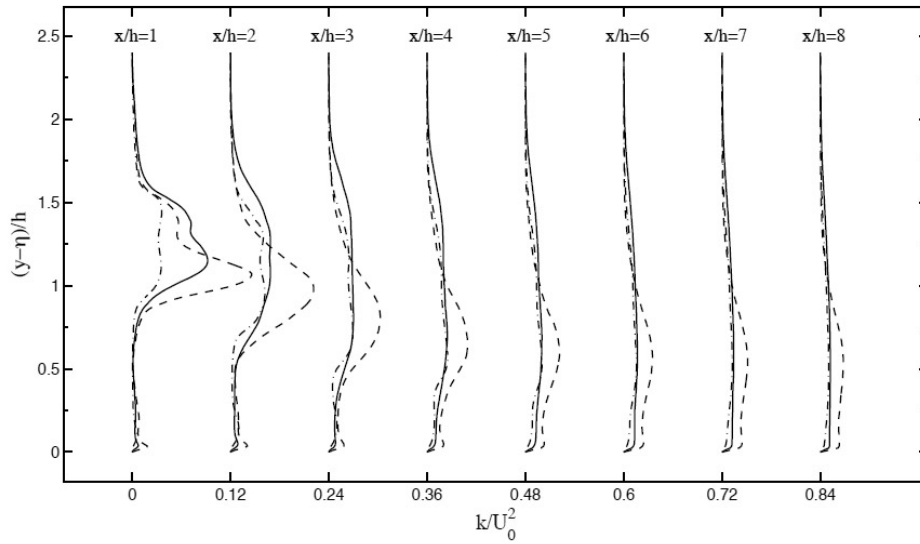
Figure 18: Turbulent kinetic energy profiles at the center plane. solid line: eddy simulation with br=1; dashed line: eddy simulation with br=1.5; dash dot: RANS with br=1

Because RANS simulations were done with the SST, eddy viscosity model, only k and Reynolds shear stress are available for comparison. They are included in figures 18 and 19 for br = 1. Aside from the immediate vicinity of the break out, the resolved kinetic energy in the eddy simulation is similar to the k profiles from the SST model.
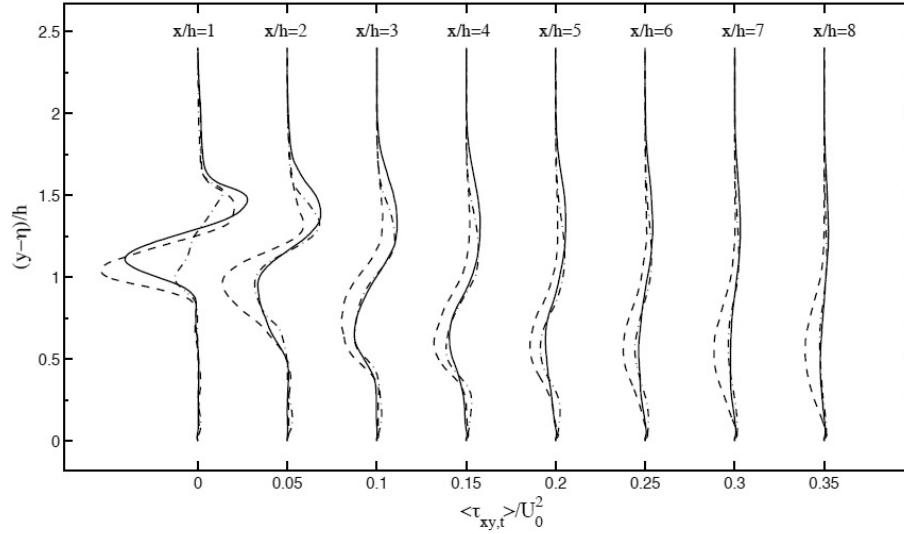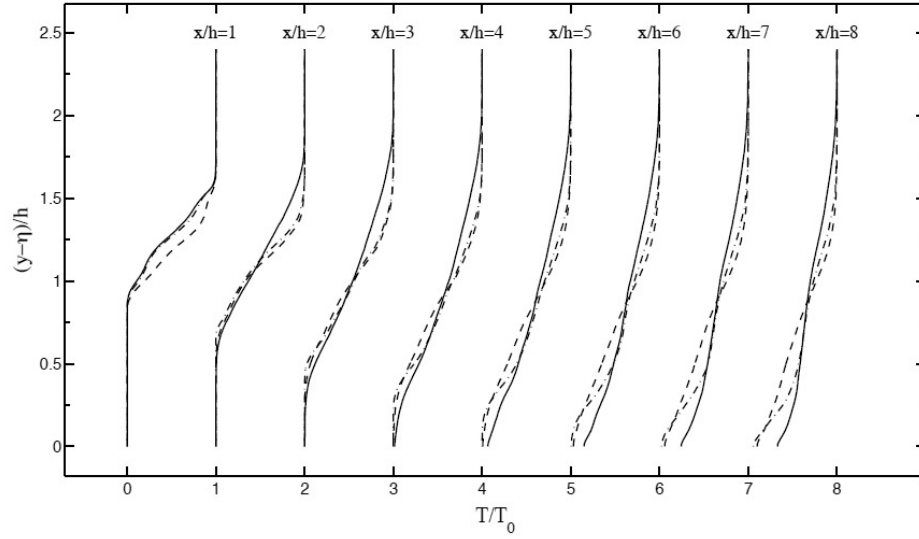

Figure 19: Turbulent shear stress profiles at the center plane. solid line: eddy simulation with br=1; dashed line: eddy simulation with br=1.5; dash dot: RANS with br=1

Most of the fluctuating kinetic energy is resolved. A comparison between resolved kinetic energy and k from the SST-SAS model is presented in Figure 20. At the present Reynolds number k is relatively small.
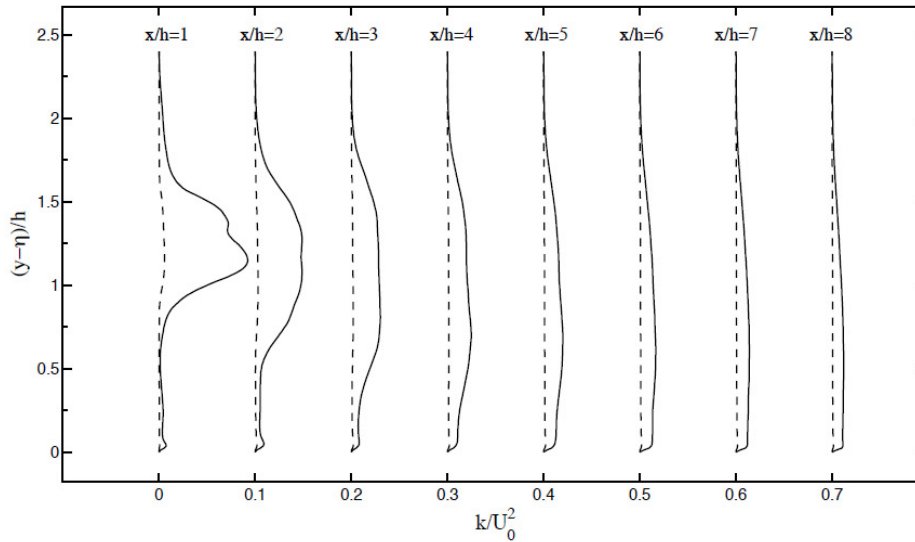
Figure 20: Resolved and modeled turbulent kinetic energy profiles of eddy simulation (br=1) at the center plane. Solid line: resolved turbulent kinetic energy; dashed line: modeled turbulent kinetic energy.

Correspondingly, the SAS viscosity is less than three times the molecular viscosity in the central region of the slot. Profiles of υ_T/υ are contained in Figure 21. Fine and base grid results are shown. As expected, the subgrid viscosity grows smaller as the grid is refined. The case with higher blowing ratio has higher υ_T but still well below RANS levels. Clearly, at the current Reynolds number, the full force of the hybrid RANS/eddy simulation character of SST-SAS is not coming into play. Rather the SAS model is functioning like an LES subgrid model.
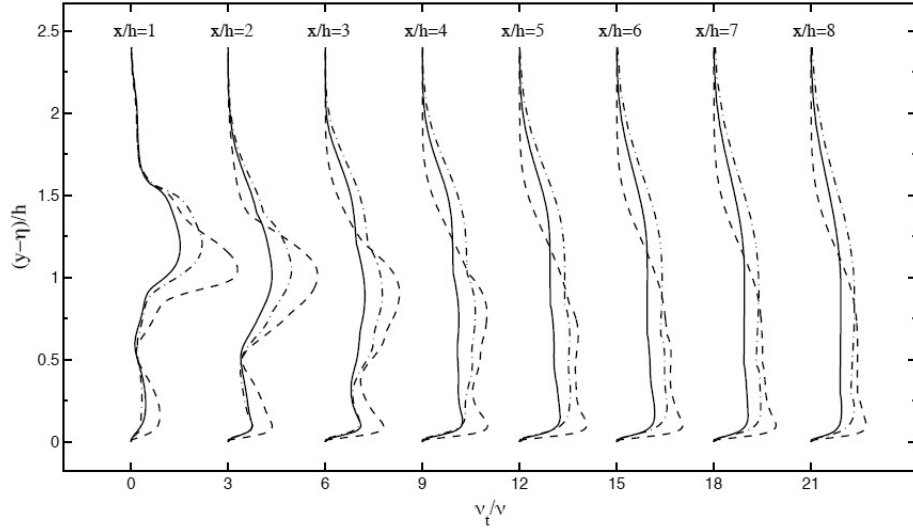
Figure 21: Ratio of eddy-viscosity to molecular viscosity profiles of eddy simulation at the center plane. solid line: fine grid case with br=1; dashed line: fine grid case with br=1.5; dash-dot: base grid case with br=1

5.2 Scalar mixing

Ultimately, we are concerned with turbulent mixing and heat transfer. Although we will refer to the 'temperature' field, a passive scalar was traced, rather than temperature, *per se*. This parallels the experimental practice of using CO_2 to study film effectiveness. Then the surface concentration is analogous to the adiabatic temperature. The analogy is exact if temperature can be treated as a passive scalar.

Mean temperature profiles in the middle of the slot are plotted in Figure 22. They have the aspect of a spreading thermal mixing layer. At the inflow, the cooling stream temperature is defined as 0 and the free stream temperature is normalized to 1.

Figure 22: Temperature profiles at the center plane. solid line: eddy simulation with br=1; dashed line: eddy simulation with br=1.5; dash-dot: RANS with br=1.

Improved predictions of film cooling effectivness are presented in Figure 23. The experimental data in these figures are for the geometry of Holloway et al. (2002a), which is similar to the present. The unsteady RANS simulation over predicts the adiabatic effectiveness, η. The decrease of η with x shows increased wall temperature. The case with higher blowing ratio provides better protection of the surface — that is, higher η — but far less than predicted (incorrectly) by unsteady RANS. The ability of the eddy simulation to predict lower effectiveness indicates that the 'anomalous' mixing is being captured. It will emerge that the cause is not the formation of the vortex loops seen in Figure 3.

br=1   br=1.5
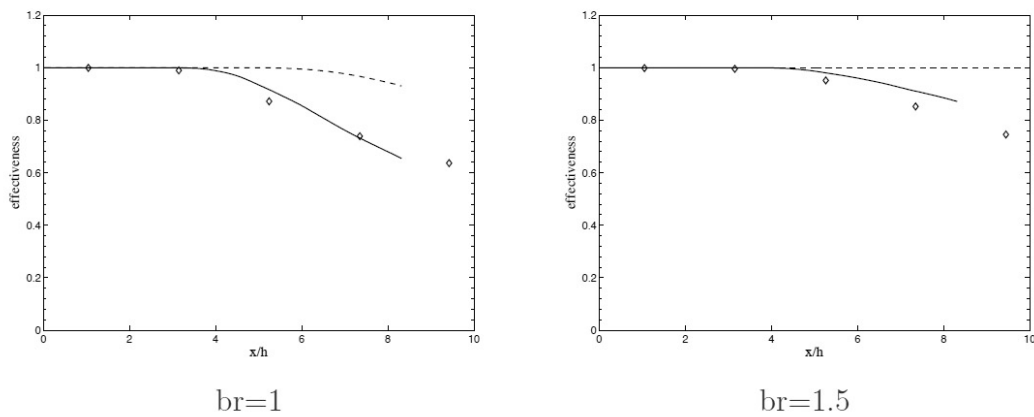
Figure 23: Film cooling effectiveness on the center line for br=1 and 1.5. Solid line: eddy simulation, dashed line: RANS (Medic & Durbin, 2005), symbols: Experiment (Holloway et al., 2002a).

Time averaged effectiveness on the wall between the lands is contour plotted in Figure 24. This shows the hot region near the trailing edge more clearly. It would be beneficial if the cooling jet did operate as in the right pane — the RANS results; unfortunately experiments are more similar to the left pane — the SST-SAS results.
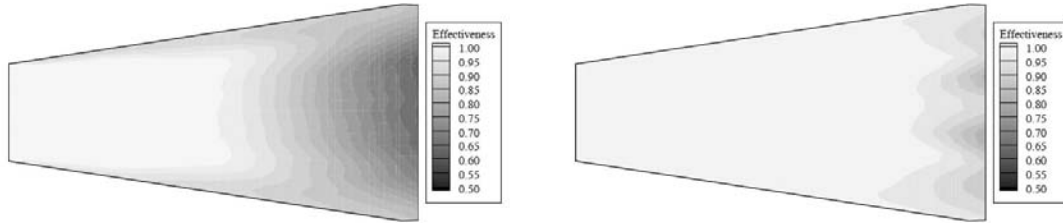
Figure 24: Film cooling effectiveness contours at the bottom wall. Left: eddy simulation with br=1, right: RANS with br=1.

Sectional views of the SAS and RANS simulations are provided in Figure 25. Curiously, the large scale undulations seen in the eddy simulation are suggestive of the ensemble average unsteadiness seen in the RANS result. Temperature is contoured in these plots, with dark being the cool fluid and white the hot. In Figure 24 the dark areas are where the lower surface is hottest; in Figure 25 this is the region toward the end of the blade surface where some white is just reaching the surface in the upper pane of Figure 25. It seems that the qualitative features of mixing within the slot are captured by the RANS simulation. But *a discrepancy to the eddy simulation appears in the mixing just next to the lower wall*; it is the cause of incorrect cooling effectiveness.
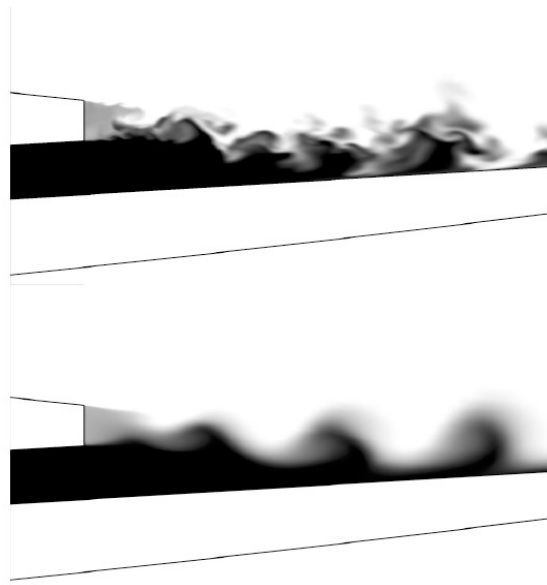
Figure 25: Instantaneous temperature contours at the center plane. top: eddy simulation with br=1 bottom : RANS with br=1.

The cooler layer next to the wall is disrupted by the large eddies in the eddy simulations, while the coherent vortex shedding does not carry hot fluid to the wall in the RANS computation. This may stem, in part, from transition in the initial separated shear layer. The RANS model assumes the layer is turbulent from the outset; in the eddy simulation the layer starts nearly laminar and becomes turbulent as three dimensional instabilities grow.

The time-averaged temperatures in Figure 26 show the diffusion of the high, freestream temperature toward the wall. The averaged effect of the eddies is to enhance diffusion; the dark region next to the wall is penetrated by gray contours in the left pane. In the lower pane the averaged effect of diffusion by Reynolds averaged vortices is too weak to mix the hotter fluid to the wall. Thus, it might be supposed that the turbulence model dissipates the vortices too strongly. It is probably more correct to say that it does not allow sufficient three-dimensionality to occur.
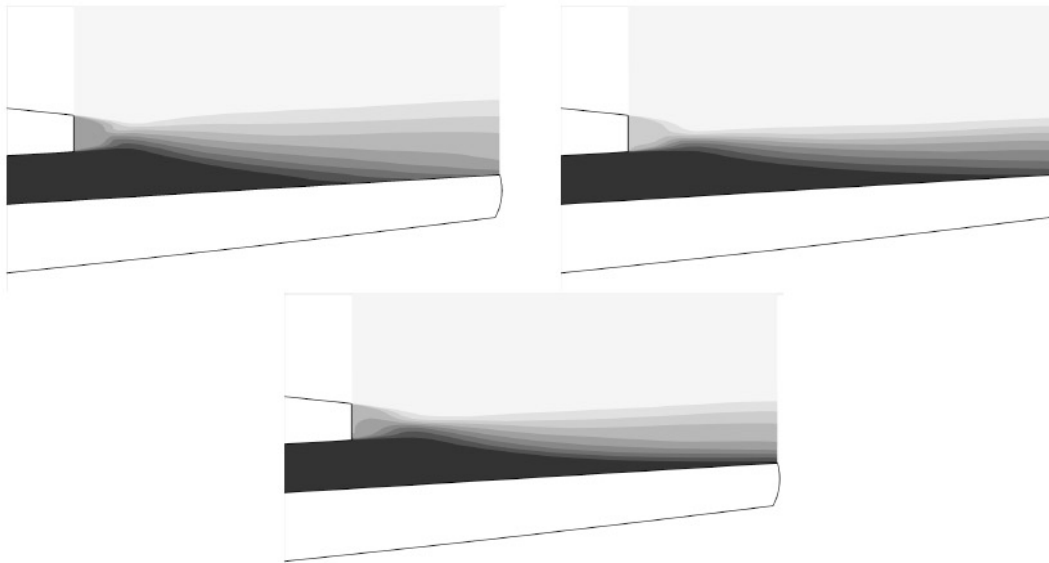
Figure 26: Mean temperature contours at the center plane. top left: eddy simulation with br=1, top right: eddy simulation with br=1.5, bottom: RANS with br=1.

Figure 27 contains end views of the temperature field in the slot at the downstream position, x = 2. There is somewhat higher mixing adjacent to the lands than in the center of the slot. In the upper most case the hotter fluid has penetrated almost to the wall on the sides of the slots.

Progressing down the slot, Figures 28 and 29 show the development of the temperature contours. Undulations of the contours for the br = 1 cases are caused by the secondary flow. The RANS results show a significant penetration of the higher temperatures into the slot flow by x = 8; they simply do not break through to the wall. Hence, the fact that η

remains near to unity is a bit misleading. The discrepancy between RANS and eddy simulation is not in the amount of mixing, but in its spatial character. It seems that the eddy viscosity model does not provide enough turbulent transport very near to the surface.
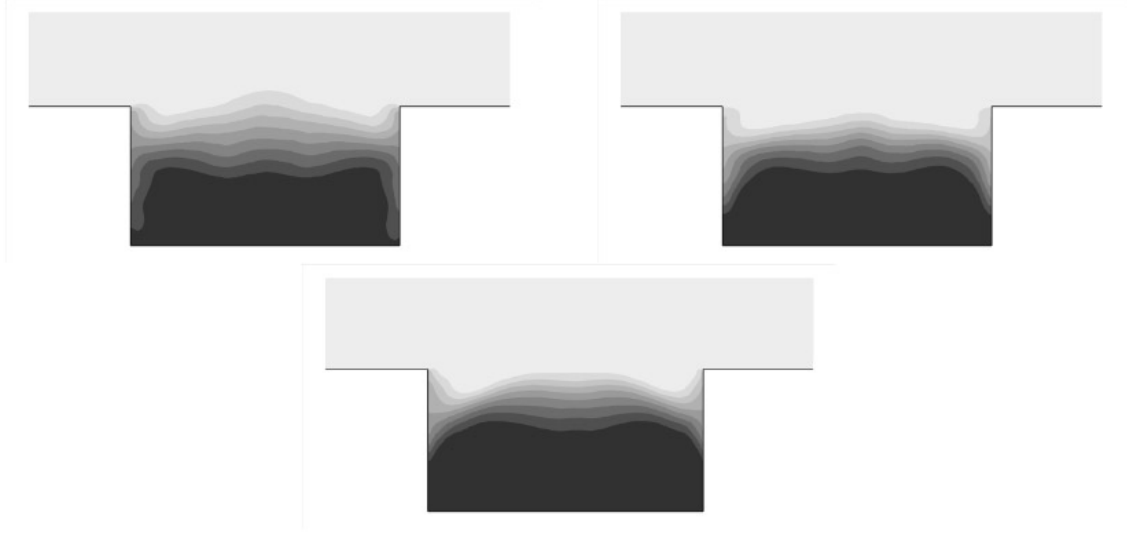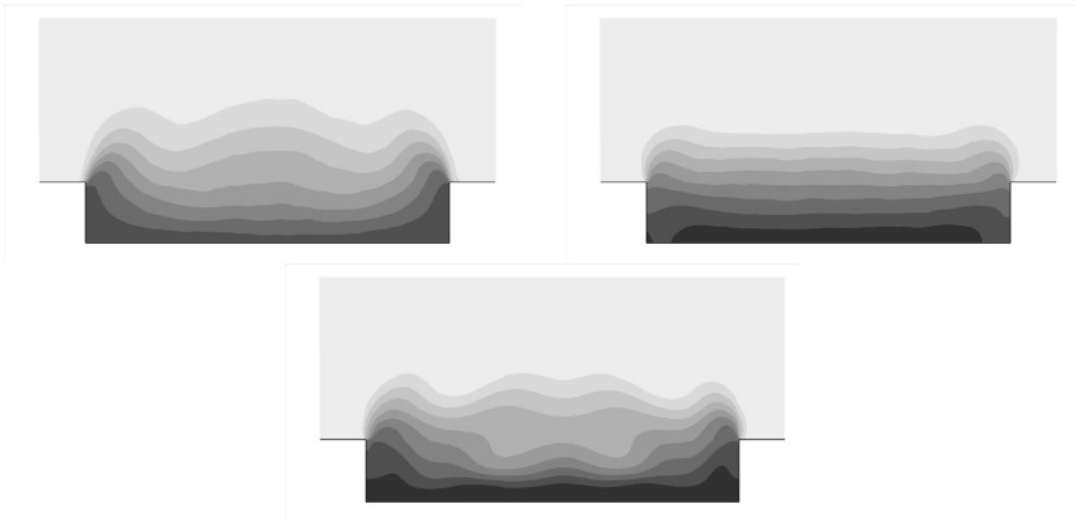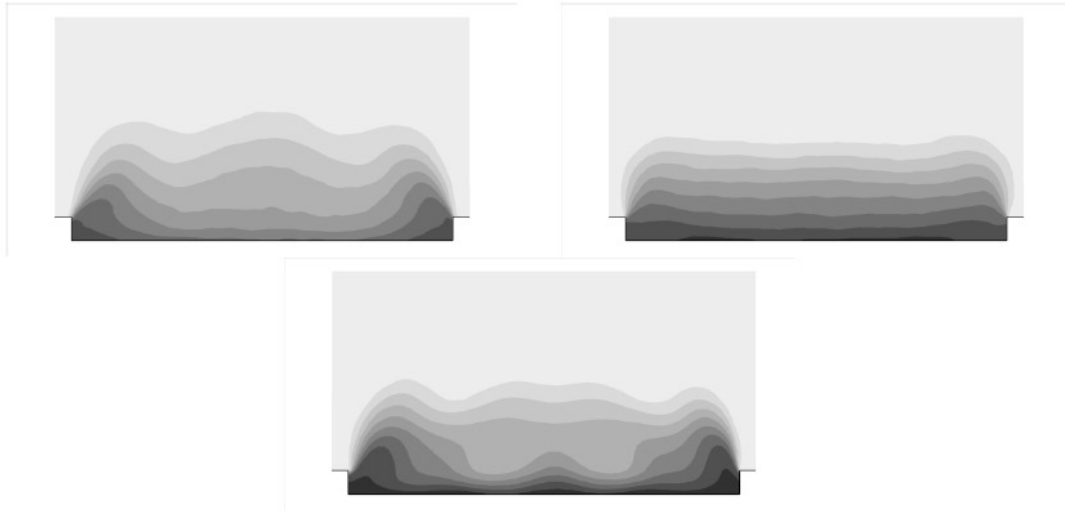

Figure 27: Mean temperature contours at x=2 plane. top left: eddy simulation with br=1, top right: eddy simulation with br=1.5, bottom : RANS with br=1.

Figure 28: Mean temperature contours at x=6 plane. top left: eddy simulation with br=1, top right: eddy simulation with br=1.5, bottom : RANS with br=1.

Figure 29: Mean temperature contours at x=8 plane. top left: eddy simulation with br=1, top right: eddy simulation with br=1.5, bottom : RANS with br=1.

Views of the instantaneous temperature contours for br = 1, at various downstream locations are contained in Figure 30. Streamwise vortices appear to mix the fluid next to the two lands. Hot fluid penetrates into those areas, leaving a tongue of cooler fluid in the middle.
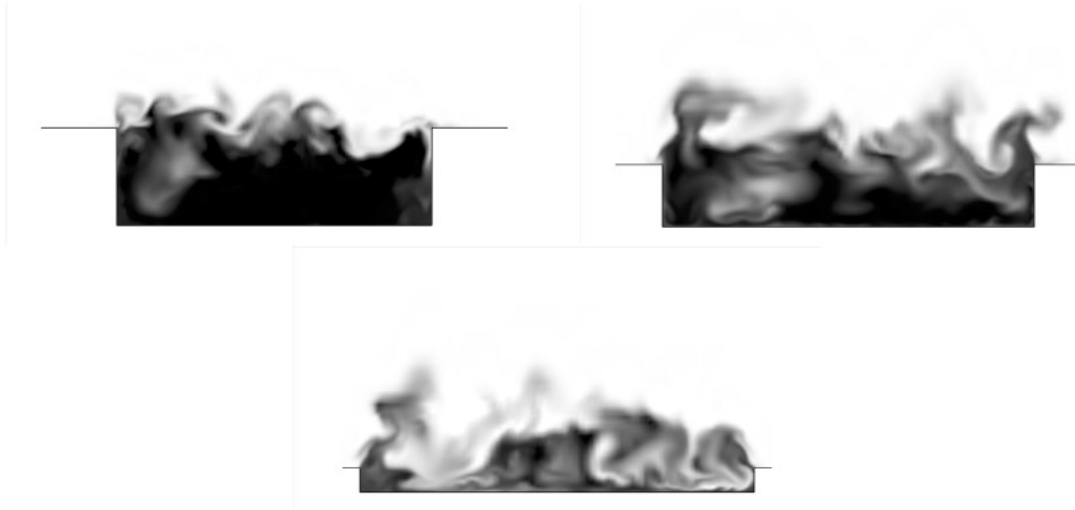
Figure 30: Instantaneous temperature contours of eddy simulation(br=1) at x-normal planes. top left: x=4, top right: x=6, bottom : x=8.

One dimensional energy spectra of velocity and temperature were calculated at selected locations within the slot. Representative spectra are presented in Figure 31. These show a peak at the non-dimensional shedding frequency of 0.37 based on the height and the bulk velocity of the slot jet: fh/U0. Recalling that the lip thickness above the slot is 0.7 times the slot height, the shedding Strouhal number is 0.26 when based on this thickness. The RANS simulation produced a Strouhal number of 0.24.

Velocity spectra at other locations were similar to those in Figure 31. Temperature spectra were more variable. Near the wall, the peak was very weak. The wall blocks eddy motions that would carry heat streaks to the wall.

A −5/3 line is included on the figures, although the Reynolds number is too low for the energy cascade to assume small scale universality. That line suggests that the numerical high frequency cut off is above the energetic turbulent scales. The velocity spectra all contain an appreciable broad band component, even those close to the lower wall.
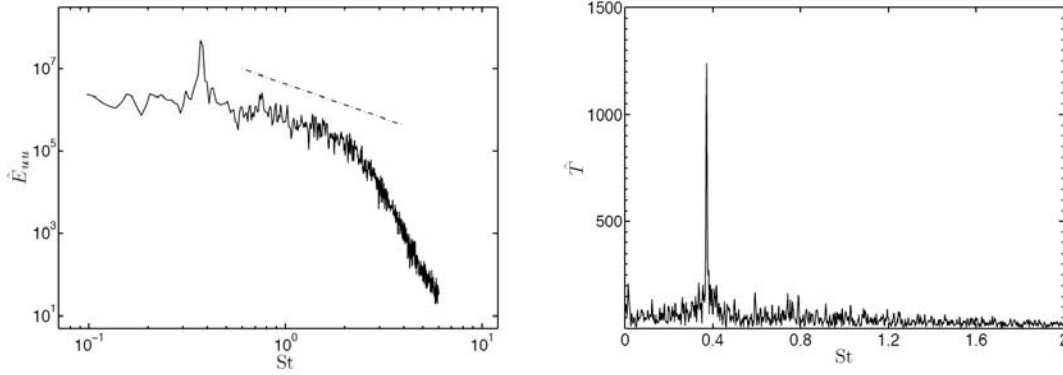
Figure 31: One dimensional streamwise energy and temperature spectra in the center plane, at x = 4, y = 0.571 for the u spectrum and y = 0.794 for the temperature spectrum. : k−5/3.

6 Results – Subsonic experiment

6.1 Velocity measurements at the trailing edge

The coordinate system for data presentation is shown in Figure 1. The streamwise (x) and cross-stream (z) coordinates are normalized by the chord length of the NACA 0012 airfoil ($c = 150$ mm). The spanwise (y) coordinate has its origin at the center of one breakout slot, and is normalized using the length between the center of the breakout slot and the land ($d = 6$ mm). Thus, $y/d = 0$ is at the center of the breakout slot and $y/d = 1$ is

at the center of the land. All PIV measurements were acquired in three different parallel planes (Figure 32), one in the center of the central breakout slot, one in the center of the land, and one in between ($y/d = 0.42$). All experiment results are normalized by the bulk average velocity $uref = 0.87$ m/s, measured 10 mm downstream of the trailing edge. Data were acquired at three different blowing ratios. The overall uncertainty of the blowing ratio is estimated to be ±0.13 by considering the uncertainty in the dimensions of the coolant exits and the uncertainty of the rotameter flow rate measurement.
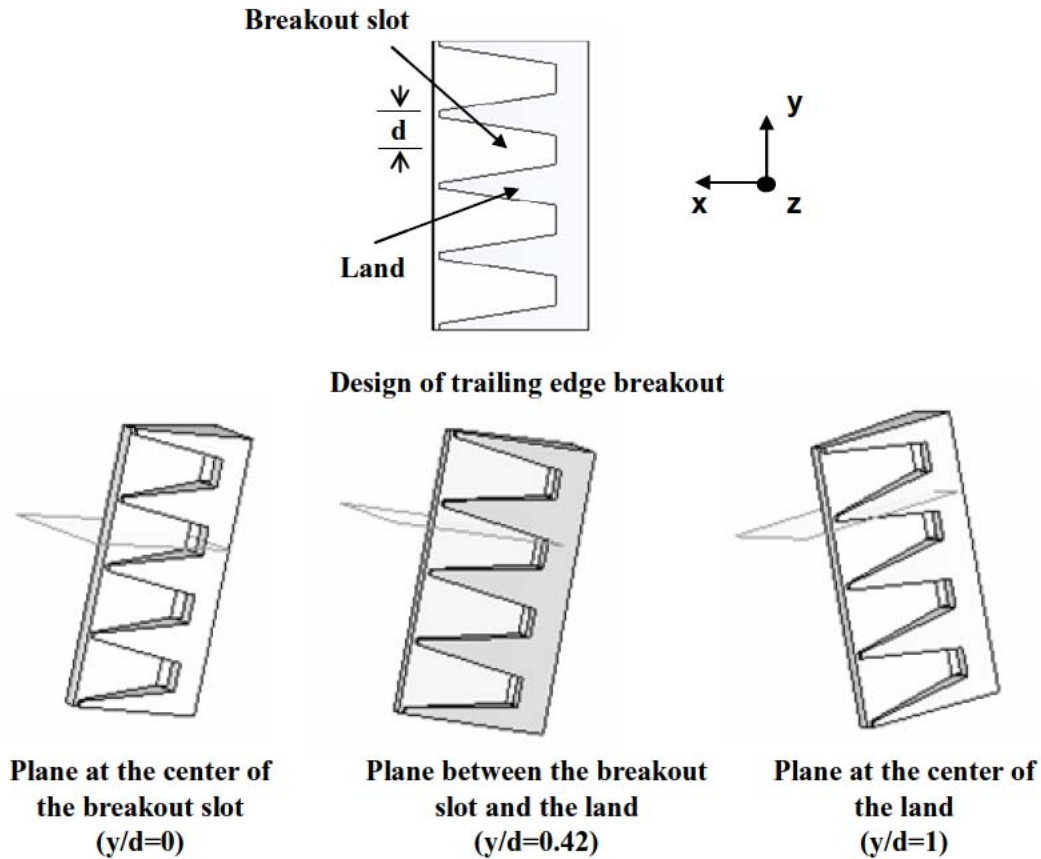
Figure 32: Trailing edge breakout coordinate system and corresponding planes for PIV measurements

Contour plots of the mean velocity magnitude around the trailing edge breakout at different blowing ratios are shown in Figures 33, 34, and 35. The black lines on each plot show the outline of the model trailing edge taken from the original SolidWorks design. The white region indicates locations where data are not available. This region extends a small distance beyond the model due to flare from the model surface that substantially degrades the PIV image quality.
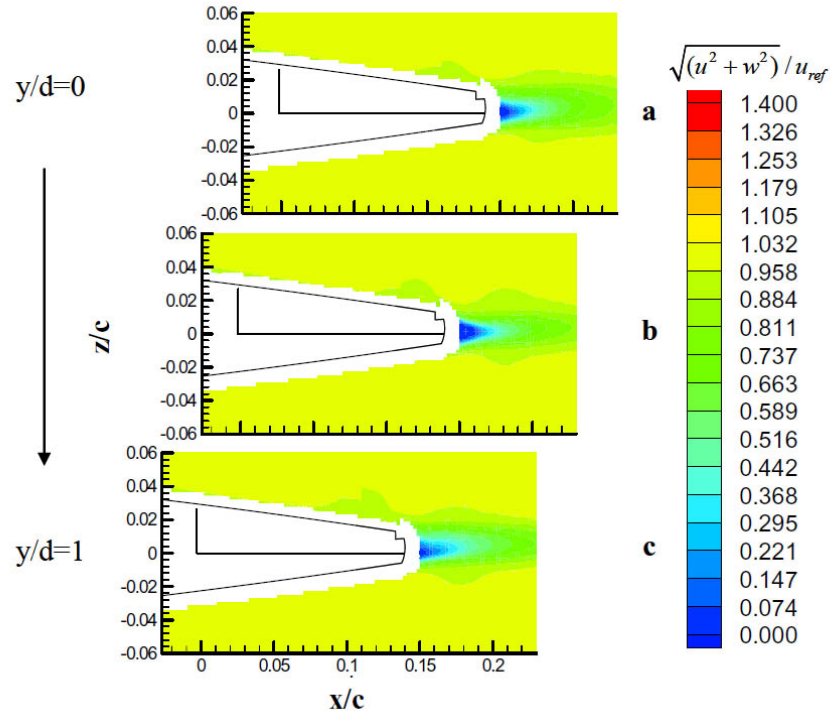
Figure 33: Contour plots of time-averaged velocity magnitude at br=0 with **a.** *y/d*=0; **b.** *y/d*=0.42; **c.** *y/d*=1
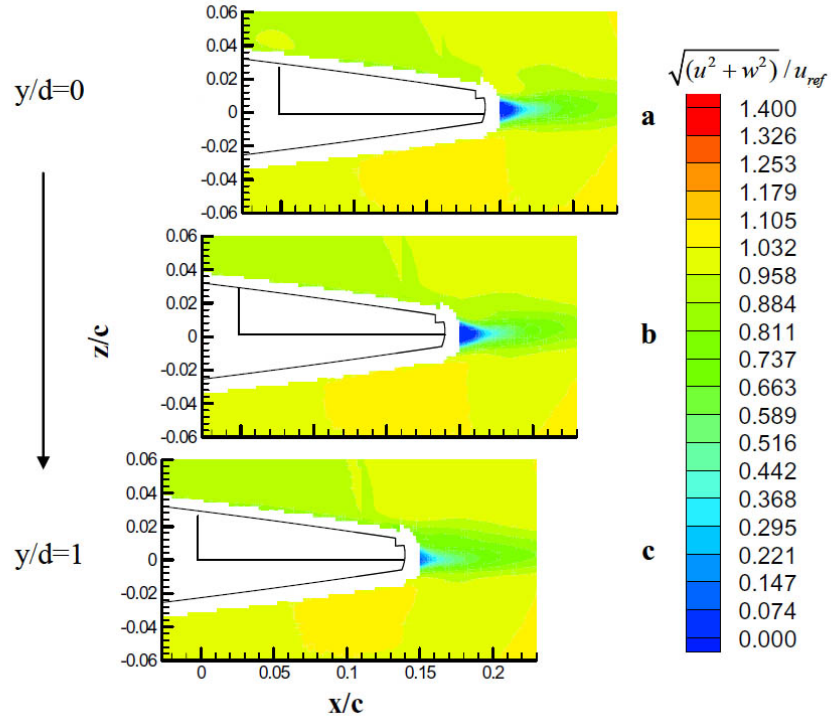

Figure 34: Contour plots of time-averaged velocity magnitude at br=1 with **a.** *y/d*=0; **b.** *y/d*=0.42; **c.** *y/d*=1
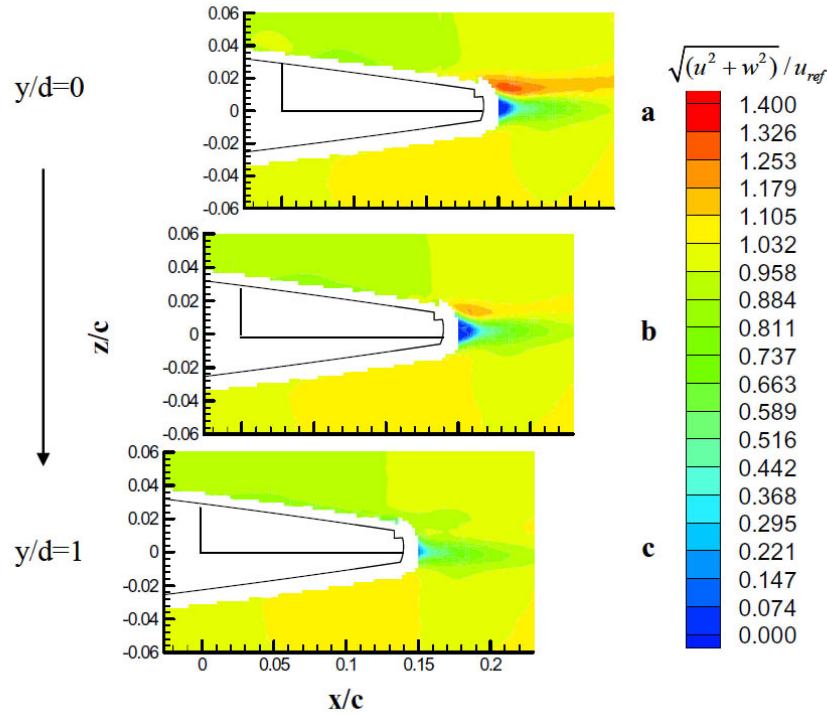
Figure 35: Contour plots of time-averaged velocity magnitude at br=1.5 with **a.** *y/d*=0; **b.** *y/d*=0.42; **c.** *y/d*=1

The br = 0 measurements shown in Figure 33 are very similar to a flow passing around a standard symmetric airfoil, which generates a symmetric wake. There is some evidence of asymmetry seen as a slightly larger velocity deficit just above the trailing edge breakout. This could be due to the asymmetric trailing edge geometry. Another possible cause could be unsteady flow moving in and out of the slot increasing the turbulent mixing on the upper surface. There is little discernable three dimensionality in the mean velocity measurements for br = 0 since the velocity field appears almost identical in the three planes.

Figures 34 and 35 show the effects of increasing blowing ratio. An obvious feature of these figures is that forced blowing induces a circulation around the airfoil. The flow speed is clearly lower on the upper (breakout) side of the airfoil than on the bottom side for br = 1. This effect is even more apparent at br = 1.5. The blowing also has a marked effect on the near wake. The wake deficit is significantly smaller at br = 1 than at br = 0, and at br = 1.5 a high speed jet is apparent, especially at *y/d* = 0. The velocity contours at the three different spanwise planes show that the mean flow structure is highly three dimensional for br = 1.5. A high speed jet is apparent on the upper side of the wake downstream of the jet center (*y/d* = 0). The jet is much weaker downstream of the land. The most important feature in the center of the land (*y/d* = 1) is the strong reduction in the size of the blue wake region just downstream of the trailing edge. This is evidence that

high speed flow is swept into the region just downstream of the land by three-dimensional flow structures.

Figures 36, 37 and 38 are plots of the *w*-velocity component extracted from the PIV measurements for three different lines of constant *z*. Figure 36a shows the *w* data measured for br = 1.5 along the line *z/c* = -0.04 in all three measurement planes. Figure 36b shows the location of this line relative to the airfoil. It is clear that the flow is very nearly two dimensional at this value of *z*. Similar results were found for the other two blowing ratios. Figure 37 which shows data along the line *z/c* = 0 (centered on the trailing edge) and Figure 38 for *z/c* = 0.01 (centered on the jet) show very significant variations with *y*. First examining Fig. 10, we see that *w* is very small at all spanwise positions when br = 0. However, increasing blowing ratio causes strong positive *w* velocity at *y/d* = 0 and 0.42 and a relatively small negative *w* for *y/d* = 1. We expect an overall positive value of *w* at *z* = 0 due to the circulation induced by the jet. At *z/c* = 0.01 (Figure 38) the overall crossstream velocity is negative as expected. As blowing increases, the velocity downstream of the land (*y/d* = 1) becomes strongly negative. Overall, the mean velocity measurements for the cases with blowing imply the existence of a pair of counter-rotating streamwise vortices as sketched in Figure 39. These would be expected to have a significant effect on mixing of the film-cooling flow with the mainstream.
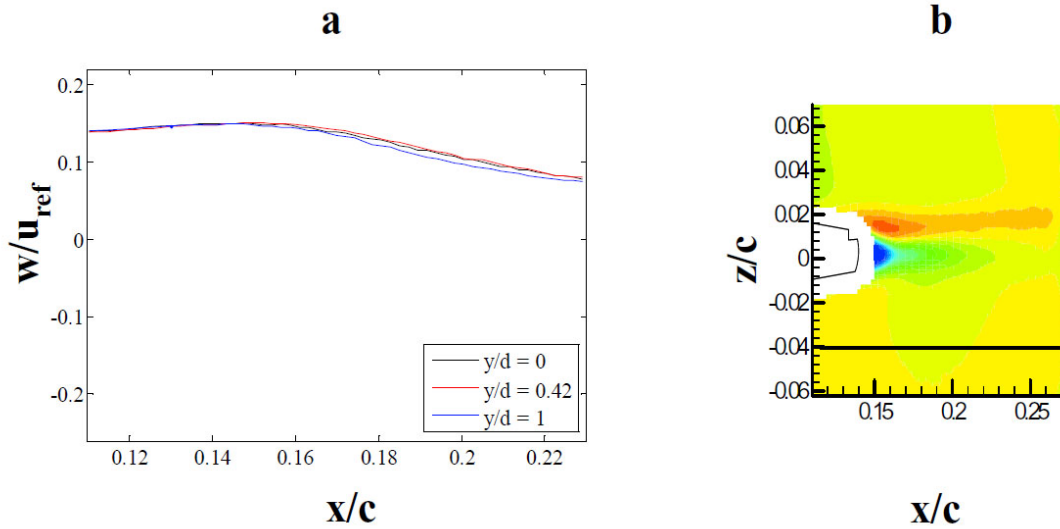

Figure 36: **a.** *w*-velocity magnitude with br=1.5 at *z/c*=-0.04; **b.** location of *w*-velocity measurements
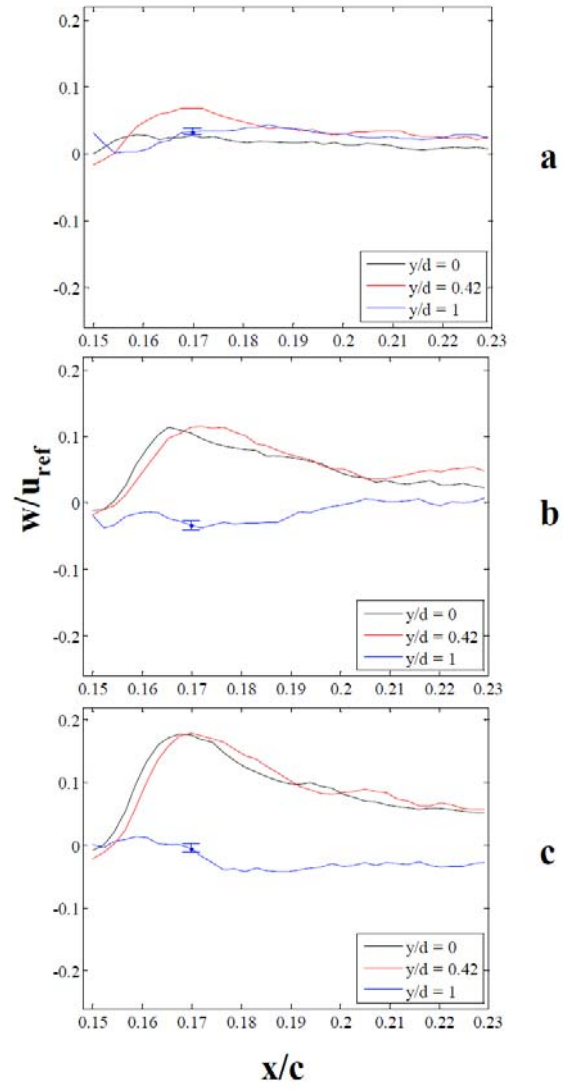
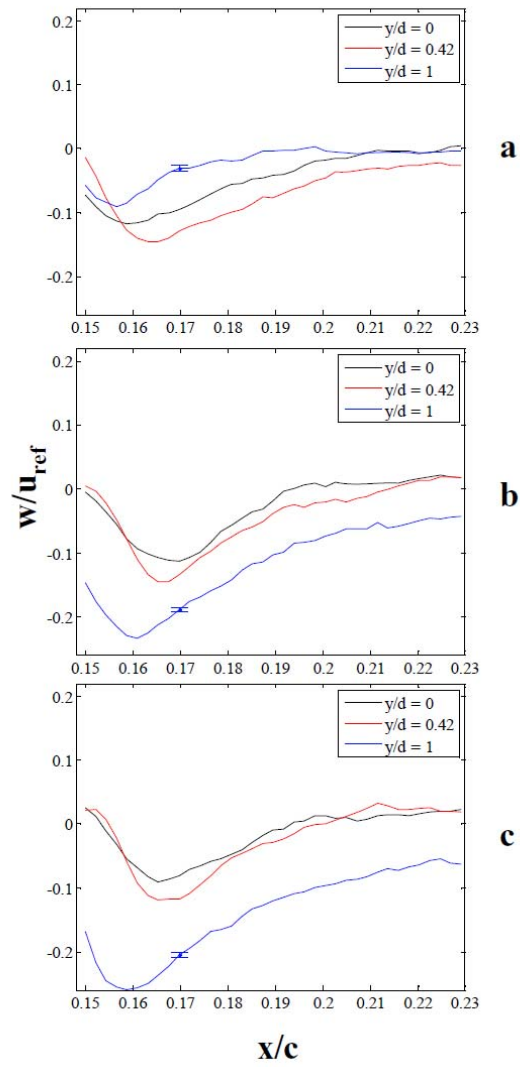Figure 37: *w*-velocity magnitude at *z/c*=0, **a.** br=0; **b.** *M*=1; **c.** *M*=1.5

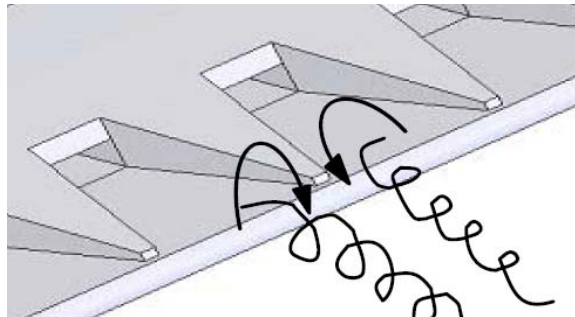Figure 38: *w*-velocity magnitude at *z/c*=0.01, **a.** br=0; **b.** br=1; **c.** br=1.5

Figure 39: Interpretation of streamwise vorticity

6.2 Turbulence measurements

Figures 40, 41, and 42 show the streamwise normal $u'u'$ component of the Reynolds stress tensor. In the plane $y/d = 0$ with br = 0 (Fig. 40a), the plot shows two local regions of high streamwise turbulence. The fluctuations in the upper region are relatively higher probably due to unsteady flow in the breakout slot. The flow at $y/d = 0.42$ (Figure 40b) shows similar characteristics since the plane is still in the region of the breakout slot, whereas $u'u'$ at plane $y/d = 1$ (Figure 40c) shows significantly lower turbulence levels. The $u'u'$ stress at the plane of the land ($y/d = 1$) is significantly lower than the other planes for all three blowing ratios indicating that the turbulence field is strongly affected by the 3D structure of the mean field.
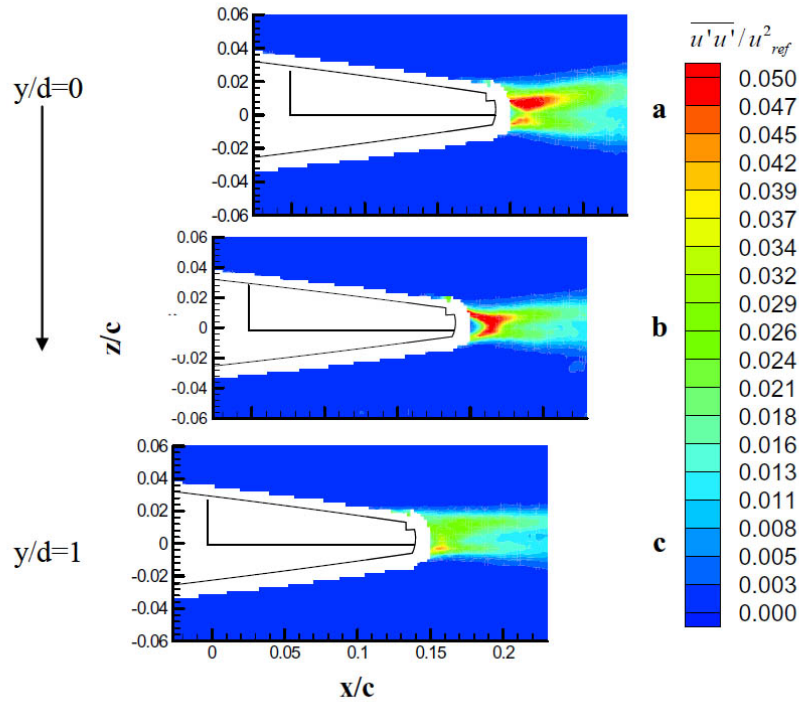

Figure 40: Contour plots of uu at br=0 with **a.** *y/d=0*; **b.** *y/d=0.42*; **c.** *y/d=1*
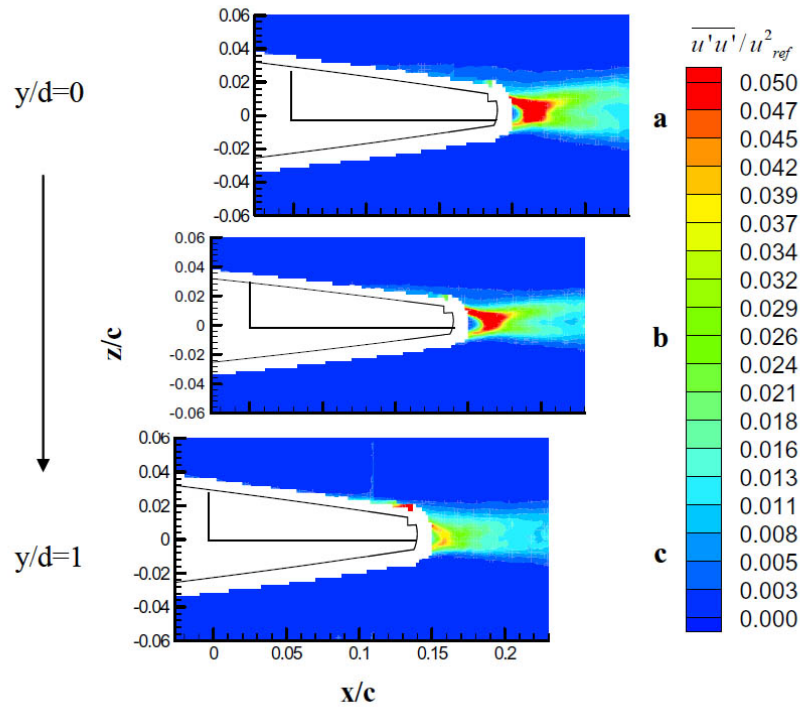
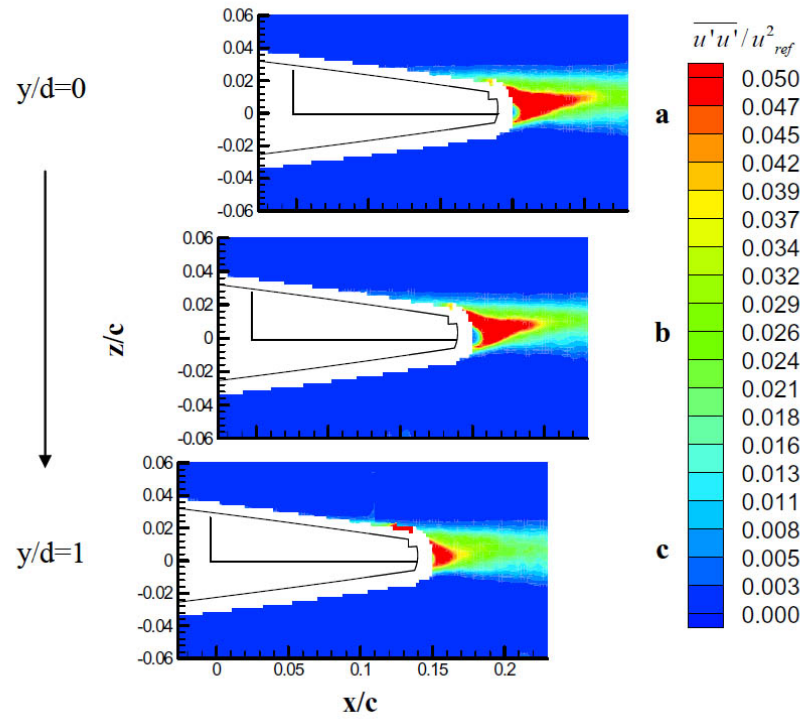Figure 41: Contour plots of uu at br=1 with **a.** *y/d=0*; **b.** *y/d=0.42*; **c.** *y/d=1*

Figure 42: Contour plots of uu at br=1.5 with **a.** *y/d=0*; **b.** *y/d=0.42*; **c.** *y/d=1*

The vertical Reynolds normal stress component, $w'w'$ is shown in Figure 43 for br = 0 and Figure 44 for br = 1.5. The br = 1 results are not shown because the structure is similar to the other two cases with the intensities lying somewhere in between. As expected for a normal wake, there is a single peak in this stress component at each streamwise location. The peak is in the center of the wake, even at high blowing ratio. There is a strong indication of three dimensionality at all three blowing ratios. The stress level is much larger downstream of the breakout as opposed to behind the land. As was also found for $u'u'$, the turbulence levels generally increase with increasing blowing ratio.
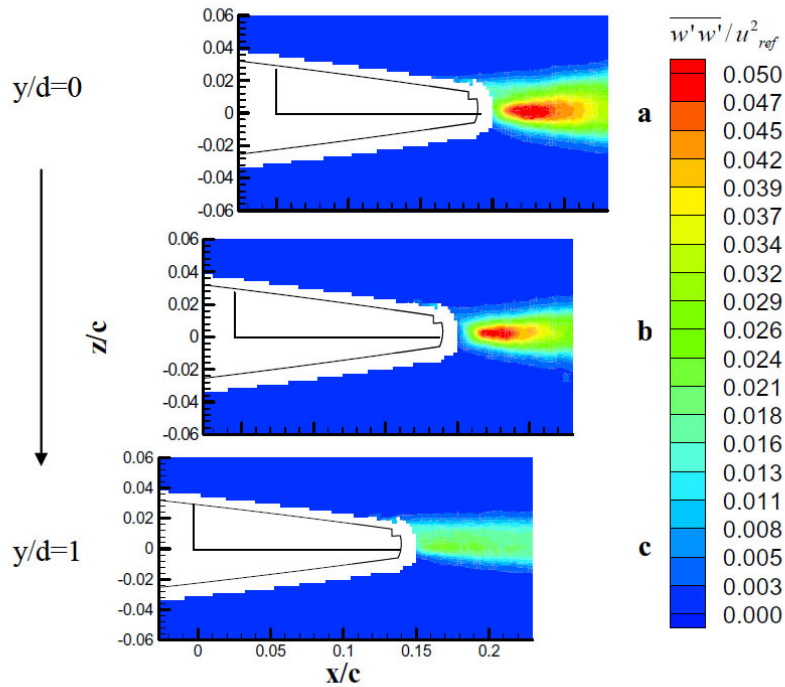

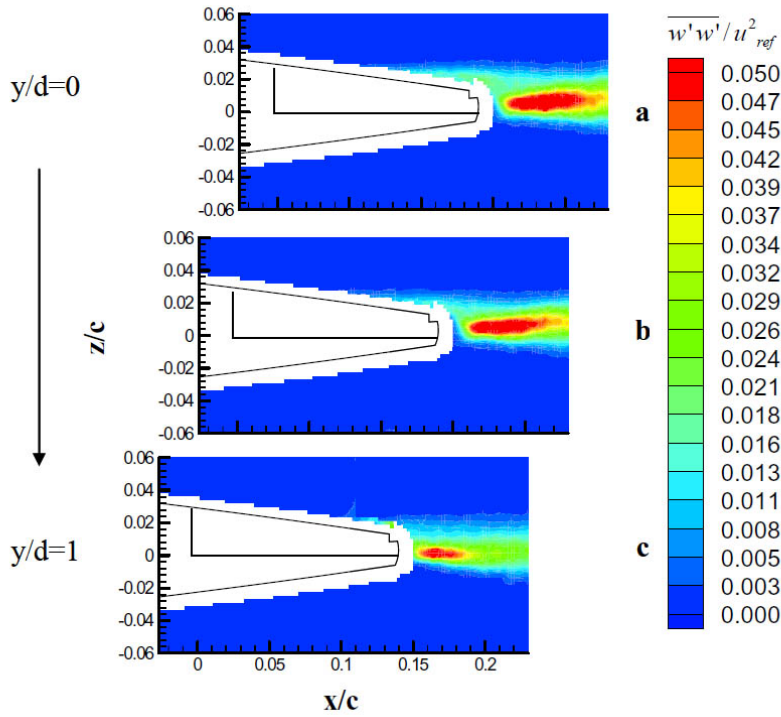Figure 43: Contour plots of ww at br=0 with **a.** *y/d=0*; **b.** *y/d=0.42*; **c.** *y/d=1*

Figure 44: Contour plots of ww at br=1.5 with **a.** *y/d*=0; **b.** *y/d*=0.42; **c.** *y/d*=1

Figures 45, 46, and 47 show the Reynolds shear stress component *u'w'*. The wake appears similar to a normal wake at br = 0. However, the region of negative *u'w'* on the upper side of the wake is somewhat larger than the opposite sign region on the bottom. This is most likely due to unsteady flow in the blowing slot which also amplified *u'u'* on the upper side of the wake. The shear stress profiles in the wake showed fairly strong sensitivity to the blowing ratio. This is most apparent at br = 1.5 where a region of strong positive *u'w'* develops above the trailing edge and extends downstream into the upper side of the wake. For blowing ratios of br = 1 and below, the three dimensional effects appear to be fairly weak. However, there is strong indication of three dimensionality at br = 1.5, where the positive peak above the trailing edge is much stronger above the jet than above the land.
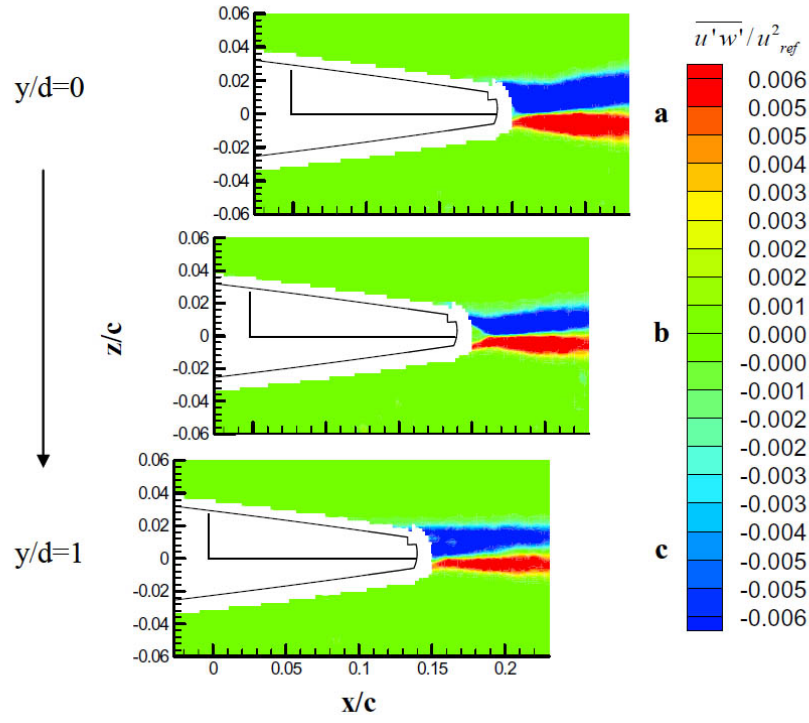
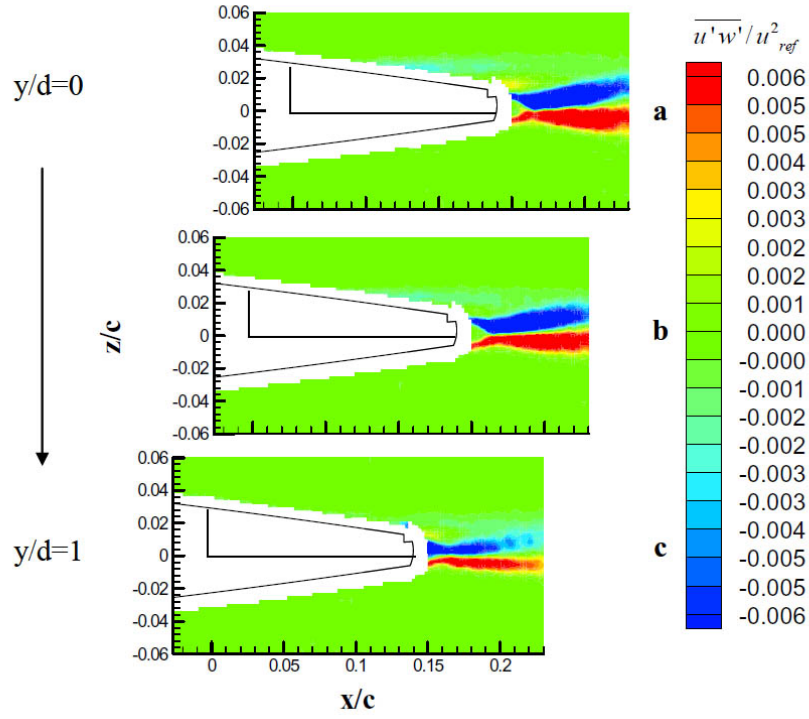Figure 45: Contour plots of uw at br=0 with **a.** *y/d*=0; **b.** *y/d*=0.42; **c.** *y/d*=1

Figure 46: Contour plots of uw at br=1 with **a.** *y/d*=0; **b.** *y/d*=0.42; **c.** *y/d*=1
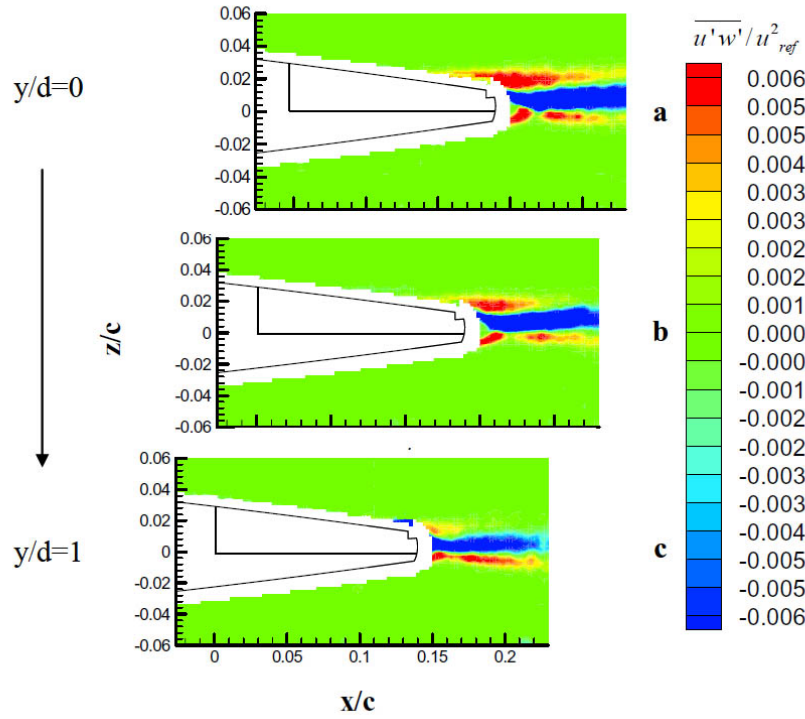
Figure 47: Contour plots of uw at br=1.5 with **a.** *y/d*=0; **b.** *y/d*=0.42; **c.** *y/d*=1

The shear stress correlation coefficient R_{uw} was calculated for each measurement plane. In most cases, the results mirrored the shear stress measurements and revealed little new about the flow. The peak correlation coefficient levels were around 0.6 indicating that the turbulence was dominated by coherent vortices formed in the free shear layers. Figure 48 shows plots of the correlation coefficient measured for br = 1. These are more revealing of the turbulence structure. Particularly at *y/d* = 0, we see four bands of negative, positive, negative and then positive correlation coefficient starting above the breakout and alternating across the near wake. On careful examination, the same features can be seen in the shear stress plot, but they are much clearer in the correlation coefficient map. The band of negative correlation coefficient above the breakout indicates that there is a shear layer with higher speed flow above lower speed flow producing negative *u'w'* or positive Reynolds shear stress. This shows that even at br = 1, the flow velocity just above the breakout is substantially lower than the mainstream flow, a clear indication of strong three dimensional mixing in this region.
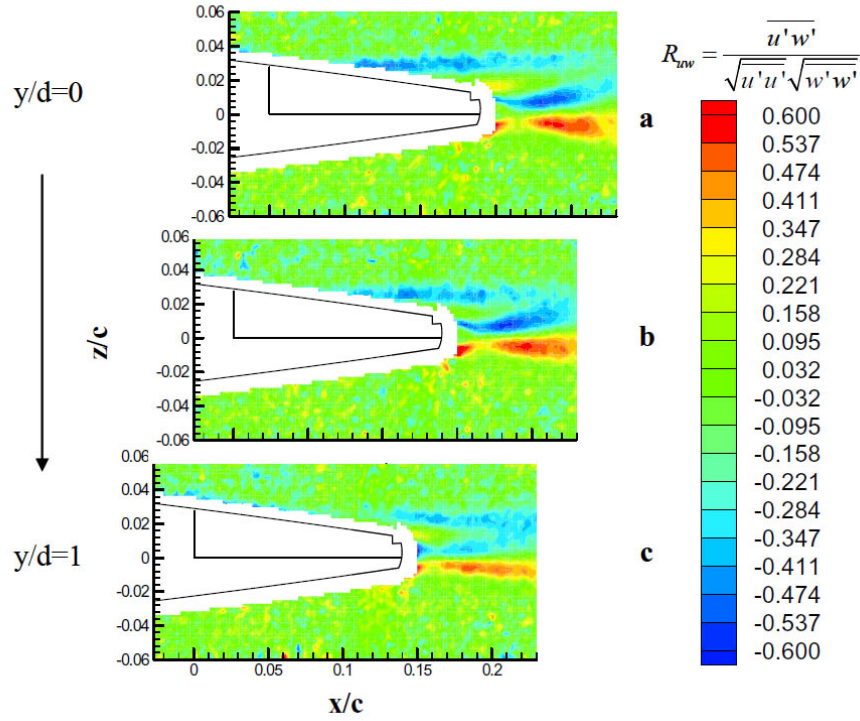
Figure 48: Contour plots of correlation coefficient R_{uw} at br=1 with **a.** y/d=0; **b.** y/d=0.42; **c.** y/d=1

Overall these results show that the presence of the cutaway trailing-edge geometry produces measurable changes in the turbulence properties even when no flow is forced through the breakout. We believe that this is due to flow moving in and out of the breakout slot in response to local turbulent pressure fluctuations. However, even with these disturbances, the flow around the trailing edge appears to be only weakly three dimensional.

Forced film-cooling flow produces strong three dimensionality in the trailing edge region, and the three dimensional effects increase in strength at the blowing ratio increases from br = 1 to br = 1.5. The mean velocity measurements indicate the presence of a pair of counter-rotating longitudinal vortices shed from the sides of the breakout lands. Also, turbulent shear stress levels above the breakout and in the wake immediately downstream of the slot jets are substantially augmented by the forced flow. Both this enhanced turbulent mixing and the three dimensional mean flow structure cause very strong mixing between the film cooling slot jets and the mainstream flow. This is responsible for the low film cooling effectiveness that has been measured in similar flows.

The flow geometry was selected specifically to enable careful comparison to detailed flow computations for the breakout. The use of a symmetric airfoil shape and the simple converging walls of the passage make the geometric specification of the flow and computational grid generation relatively simple compared to a full turbine cascade. The

flow acceleration produced by the converging inserts keeps the airfoil boundary layers thin as they would be in a real turbine. The breakout geometry is fully representative of modern turbine geometries including the blunt trailing edge on the airfoil, the blunt lip of the slot jet, and the tapered lands between the slot jets. Therefore, we believe that this flow captures realistic three dimensional flow features that cause the low film cooling effectiveness experienced in actual turbines.

It would be desirable to include full field velocity measurements fully defining all of the flow features including those blocked from view by the lands in the present experiments. However, the near wake is thoroughly documented and shows strong three-dimensional features. By comparing these measurements to computations, it should be possible to determine which models are capturing the correct features of the breakout flow based on which are producing the correct near-wake behavior.

7 Results – Transonic experiment

At present the only data available for the transonic rig are pressure data and preliminary PIV measurements. The pressure measurements for the wing without breakouts and the breakout wing at br=0 are shown in Figure 49 below.

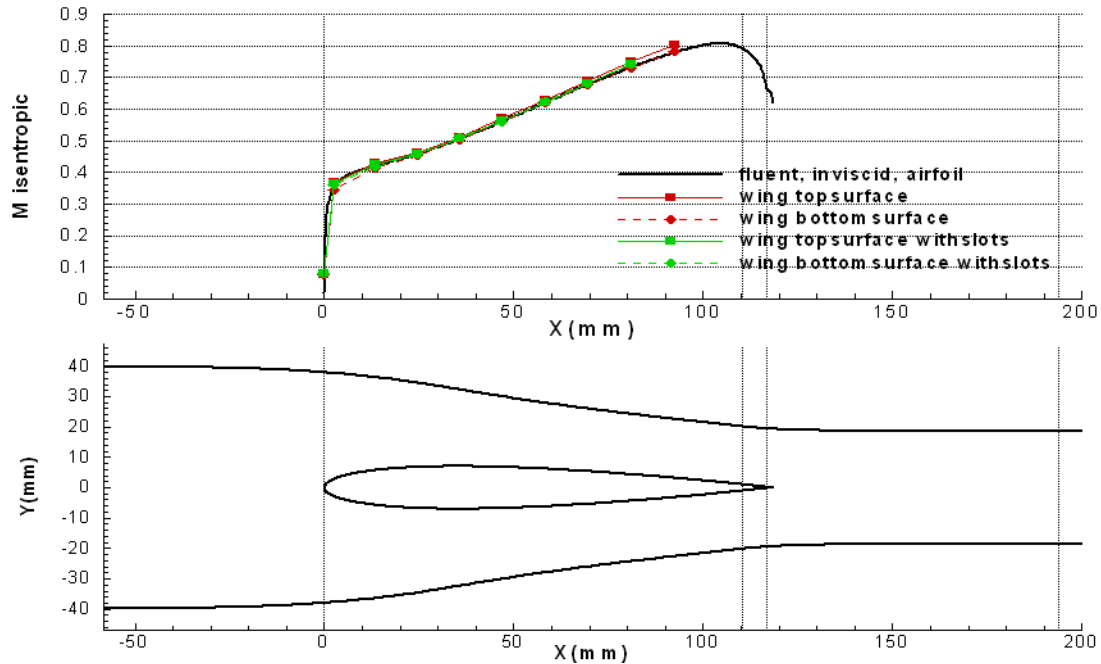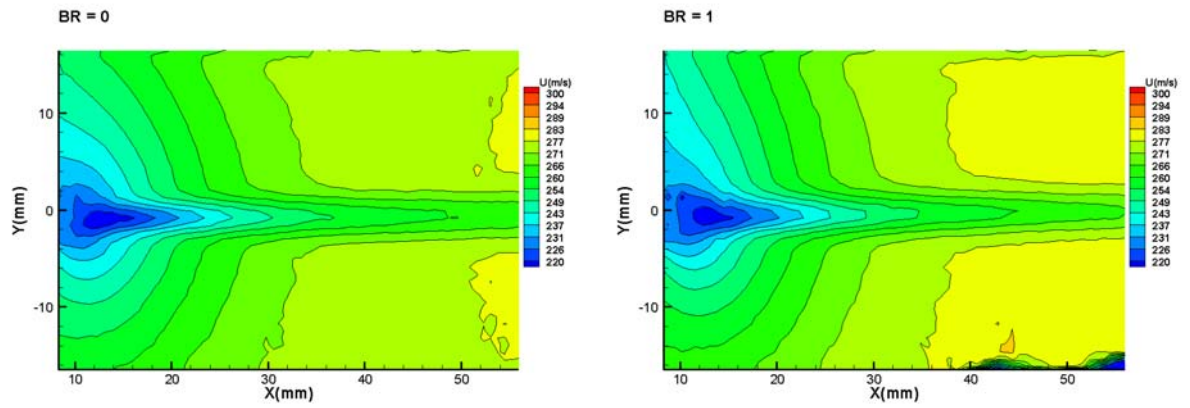Figure 49: Pressure measurements for the slotted and unslotted wings at br=0. solid line shows design CFD calculation

The measurements are in good agreement with the CFD, indicating that the wind tunnel successfully produces the desired pressure distribution on the wing. The one exception is the slight asymmetry near the trailing edge of the unslotted wing (shown in red). This is
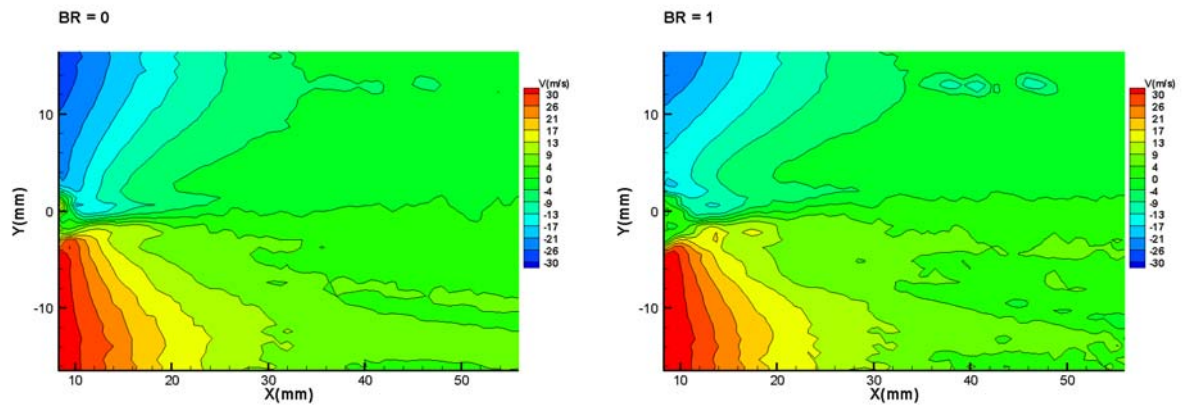
most likely due to asymmetry of the SLA part, which came out with a small but visible taper in the spanwise direction.

Preliminary PIV measurements are shown in Figure 50, and the location of these measurements is shown in Figure 51. These measurements cover nearly the entire width passage right after the trailing edge.

U, br=0

U, br=1

V, br=0

V, br=1

uu, br=0   uu, br=1

vv, br=0   vv, br=1
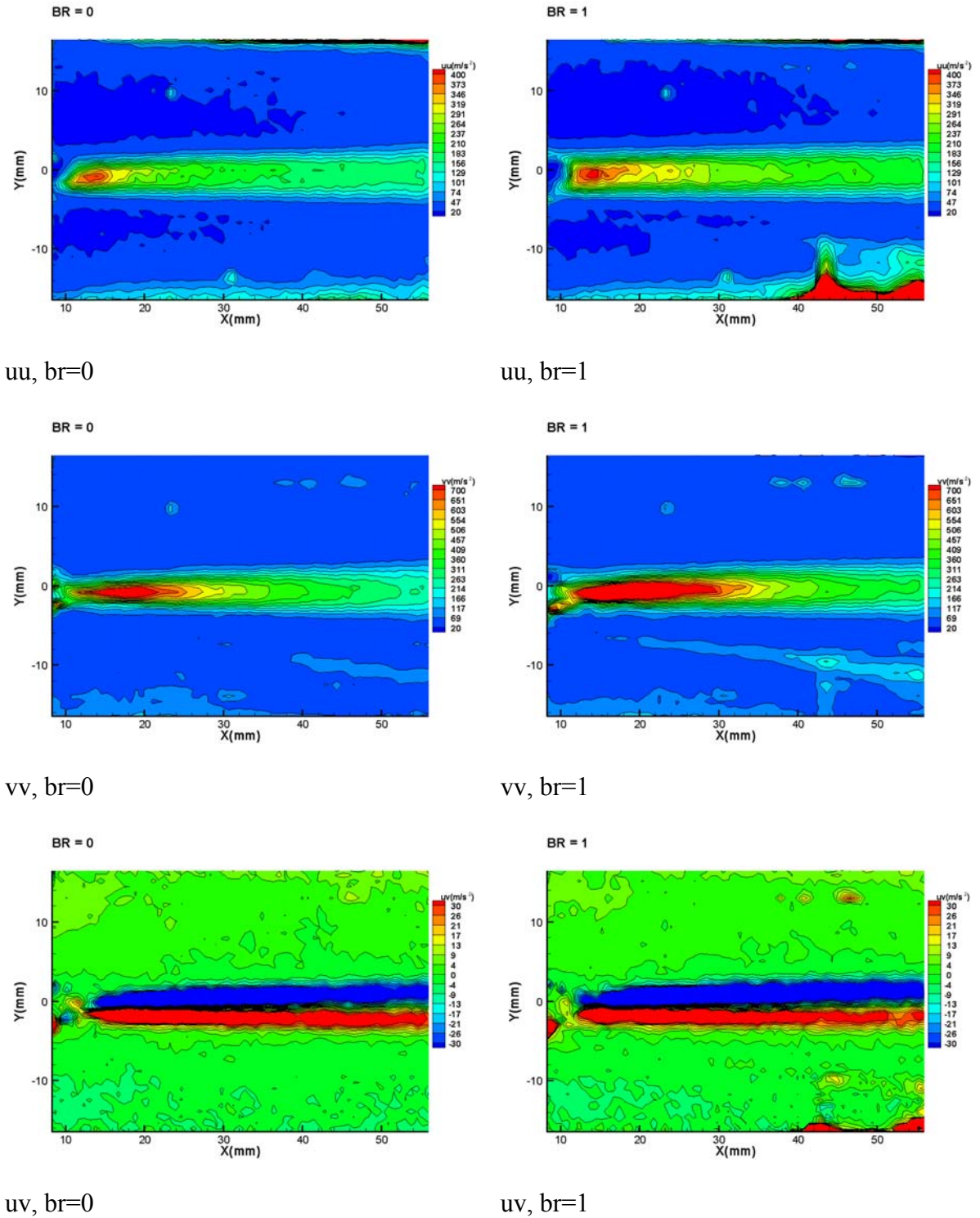
uv, br=0   uv, br=1

Figure 50: Preliminary PIV measurements for the slotted wing at br=0 (left) and br=1 (right) along the slot centerline.
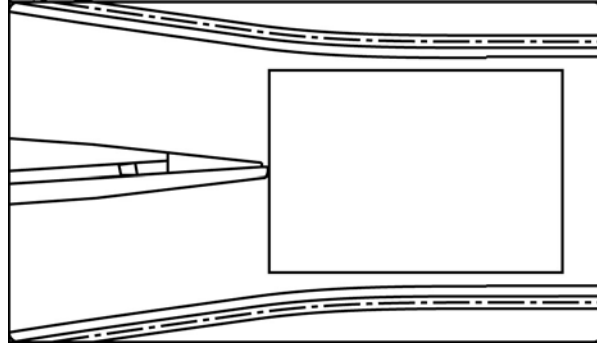
Figure 51: Location of preliminary PIV measurement window relative to wing and wall geometry.

These measurements are only preliminary because (1) more image pairs are needed for converged statistics, and (2) some of the image pairs were contaminated by glare from a mid-run burn in the plastic walls. Nonetheless, some observations may be made from these results. Along the center plane, increasing the coolant velocity increases the overall velocity more uniformly (in the vertical direction) than for the subsonic case, and the changes in turbulent stresses are not as obvious in the near-wake here as they are for the subsonic case. This indicates that higher resolution will be needed to observe the flow features of interest for the transonic experiment. With our PIV setup we can achieve resolution up to four times that shown above. However, most likely it will not be possible to obtain measurements in the interior section of the slot between lands.

8. Summary
Improved cooling of turbine blade trailing edges is required in order to operate engines at higher turbine inlet temperature with reduced cooling flow requirements. A breakthrough in understanding and modeling the flow in the trailing edge region has been made using a coupled set of experiments and simulations. The detached-eddy-simulation (DES) method had been adapted to the trailing-edge breakout flow using detailed experimental data to guide the implementation. Implementation of the inflow boundary conditions required particular care. The results show that the flow contains strong coherent vortices that carry hot freestream fluid all the way to the metal surface of the turbine blade. The effects of these vortices are not captured by RANS or URANS simulations. The DES methodology developed here can now be used to design improved breakout geometries to reduce the strength of the coherent vortices. A second transonic experiment has been developed to provide additional empirical backup for simulations at realistic Mach and Reynolds numbers. Only preliminary data from that experiment are available to date.

References

[1] D.S. Holloway, J.H. Leylek, and F.A. Buck Pressure-Side Bleed Film Cooling: Part 1, Steady Framework for Experimental and Computational Results. ASME Turbo Expo 2002   GT2002-30471.

[2] D.S. Holloway, J.H. Leylek, and F.A. Buck Pressure-Side Bleed Film Cooling: Part 2, Unsteady Framework for Experimental and Computational Results. ASME Turbo Expo 2002   GT2002-30472.

[3] G. Medic and P. Durbin, Unsteady Effects on Trailing Edge Cooling, Journal of Heat Transfer, 2005, 127, pp. 388-392.

[4] F. R. Menter and Y. Egorov, A Scale-Adaptive Simulation Modeling using Two-Equation Models, AIAA paper 2005-1035.

[5] O. Uzol and C. Camci Uzol Aerodynamic Loss Characteristics of a Turbine Blade with Trailing Edge Coolant Ejection: Part 1 – Effect of Cutback Length, Spanwise Rib Spacing, Free-Stream Reynolds Number, and Chordwise Rib Length on Discharge Coefficients. Journal of Turbomachinery 123: 238-248.

[6] Martini, P., Schultz, A., Whitney, C. F. & Lutum, E. 2004 Experimental and numerical investigation of trailing edge film cooling downstream of a slot with internal rib arrays. Journal Of Turbomachinery 126, 229–236.

[7] Martini, P., Schultz, A. & Bauer, H. J. 2006 Film cooling effectiveness and heat transfer on the trailing edge cut-back of gas turbine airfoils with various internal cooling designs. Journal of Turbomachinery 128, 196–205.

[8] Van der Weide, E., Kalitzin, G., Schl¨uter, J. & Alonso, J. 2006 Unsteady turbomachinery computations using massively parallel platforms. AIAA Paper 2006-421.

[9] Jameson, A. 1985 Transonic flow calculations for aircraft, lecture notes in mathematics. Numerical Methods in Fluid Dynamics 1127, 156–242.

[10] Menter, F. R. 1992 Two-equation eddy-viscosity turbulence models for engineering applications. AIAA Journal 32, 1598–1605.

[11] Menter, F. R. & Egorov, Y. 2005 Self-adaptive simulation of aerodynamic flows. Tech. Rep.. ANSYS.

[12] Menter, F. R., Kuntz, M. & Bende, R. 2003 A scale-adaptive simulation model for turbulent flow predictions. AIAA Paper 2003-0767.

[13] Barth, T. & Jespersen, D. 1989 The design and application of upwind schemes on unstructured meshes. AIAA Paper 89-0366.

[14] Kang, S. & Choi, H. 2002 Suboptimal feedback control of turbulent flow over a backward-facing step. Journal of Fluid Mechanics 463, 201–227.

[15] Lund, T. S., Wu, X. & Squires, K. D. 1998 Generation of turbulent inflow data for spatially-developing boundary layer simulation. Journal of Computational Physics 140, 233–258.

[16] Joo, J. 2008 Eddy simulation of turbine blade trailing edge cooling. PhD thesis, Stanford University.

[17] A. Vicharelli and J. K. Eaton, Turbulence Measurements in a Transonic Two-Passage Turbine Cascade, Experiments in Fluids, Vol 40, 2006, pp. 897-917.

Appendix A – Personnel Supported During Duration of Grant

Yude Chen	Graduate Student, Stanford University
	MS 2006, Currently employed by Sun Microsystems
Jongwook Joo	Graduate Student, Stanford University
	PhD 2008, now Post-doc at Iowa State University
Claude Matalanis	Graduate Student, Stanford University
	PhD 2007, Currently employed by UTRC
Amanda Vicharelli	Graduate Student, Stanford University
	Ms 2004, continuing PhD
Alex Wood	Graduate Student, Stanford University
	MS 2005, Currently employed by: Quatrotec Inc.
Paul A. Durbin	Professor, Iowa State University
John K. Eaton	Professor, Stanford University

Appendix B – Publications

A. Vicharelli and J. K. Eaton, Turbulence Measurements in a Transonic Two-Passage Turbine Cascade, Experiments in Fluids, Vol 40, 2006, pp. 897-917.

Y. Chen, C.G. Matalanis, and J.K. Eaton, High Resolution PIV Measurements Around a Model Turbine Blade Trailing Edge Film-Cooling Breakout, Proc. of 5th Int. Symp. on Turbulence and Shear Flow Phenomena, Munich, Aug. 2007.

Y. Chen, C.G. Matalanis, and J.K. Eaton, High Resolution PIV Measurements Around a Model Turbine Blade Trailing Edge Film-Cooling Breakout, *Experiments in Fluids*, Vol. 44, 2008, pp. 199-209.

J. Joo *Eddy Simulation of Turbine Blade Trailing Edge Cooling*. PhD thesis, Stanford University, 2008.